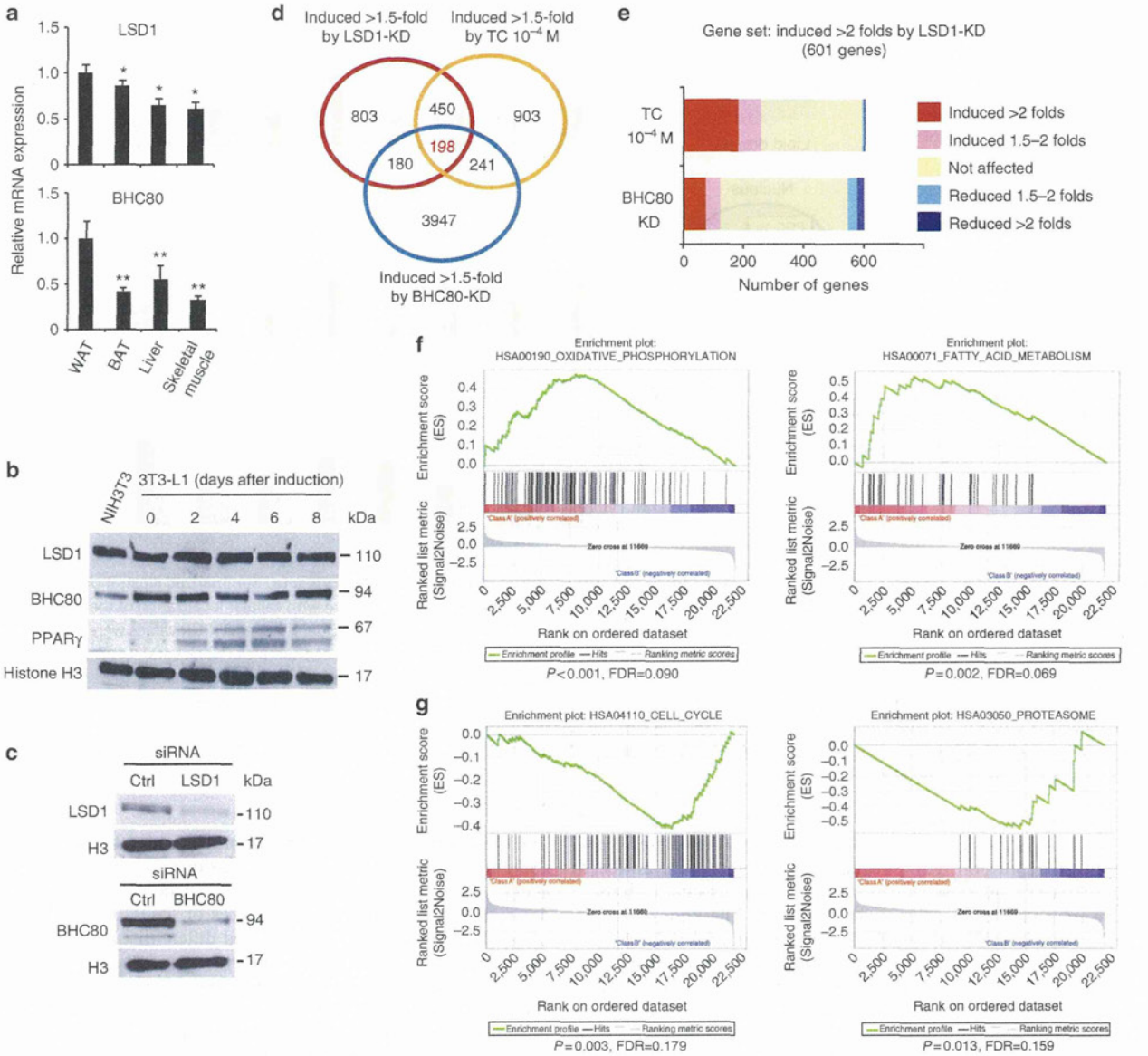

Figure 1 | Genome-wide analyses of LSD1-regulated genes in adipocytes. (**a**) Preferential expression of LSD1 and BHC80 in WAT. Expression of *LSD1* and *BHC80* mRNAs in epididymal WAT, interscapular BAT, liver and skeletal muscle. 13-week old C57BL/6J mice were fasted for 16 h before tissue dissection. Quantitative RT-PCR values were normalized to the expression levels of the housekeeping *36B4* gene, and are shown as means±s.d. of four mice. $^{*}P<0.05$, $^{**}P<0.01$ versus WAT by Student's *t*-test. (**b**) The protein expression of LSD1 and BHC80 in adipogenic 3T3-L1 cells. The cells were subjected to adipogenic induction as described in Methods, and were collected at the indicated time points. (**c**) Specific siRNA-mediated knockdown of LSD1 and BHC80 in 3T3-L1 cells. *In silico* analysis, using mouse genome and EST databases, confirmed the target specificities of the siRNAs. For western blot analysis, protein samples were prepared 72 h after siRNA introduction. (**d**) Venn diagram of the genes induced 1.5-fold or more by LSD1-knockdown (KD), BHC80-KD or TC treatment. siRNA-introduced or TC-treated 3T3-L1 cells were subjected to adipogenic induction for 24 h. Control siRNA or vehicle-treated samples were used as controls. (**e**) Unidirectional effects of TC and BHC80-KD on LSD1-target genes. (**f**) Gene set enrichment analysis of commonly upregulated genes by LSD1-KD, BHC80-KD and TC treatment. In each panel, nominal *P*-values and false discovery rates (FDRs) are indicated. (**g**) Gene set enrichment analysis of commonly downregulated genes by LSD1-KD, BHC80-KD and TC treatment. Significantly enriched gene sets are shown. Nominal *P*-values and FDRs are indicated.

the transcription start site of the *PGC-1α* promoter (sites 3 and 4) (Fig. 3a). Similarly, the selective occupancy of LSD1 was observed at the *PDK4*, *FATP1* and *ATGL* gene promoters but not at the *actB* gene promoter (encoding β-actin) (Fig. 3b). The enrichment of di/tri-methylated H3K4 as well as acetylated H3 was enhanced by LSD1-KD at LSD1-bound promoters, whereas the *actB* promoter remained unchanged (Fig. 3c,d). Moreover, *Pdx1* gene, which is not expressed in adipose cells, showed enriched LSD1 occupancy and the increased H3K4 methylation after LSD1-KD, emphasizing the close relationship between LSD1 and H3K4 demethylation in energy-expenditure genes (Fig. 3b,c). Di-methylated H3K4 was enriched at the *PGC-1α* promoter under the TC treatment (Fig. 3e), consistent with the inhibition of LSD1-dependent demethylation by TC.

© 2012 Macmillan Publishers Limited. All rights reserved.

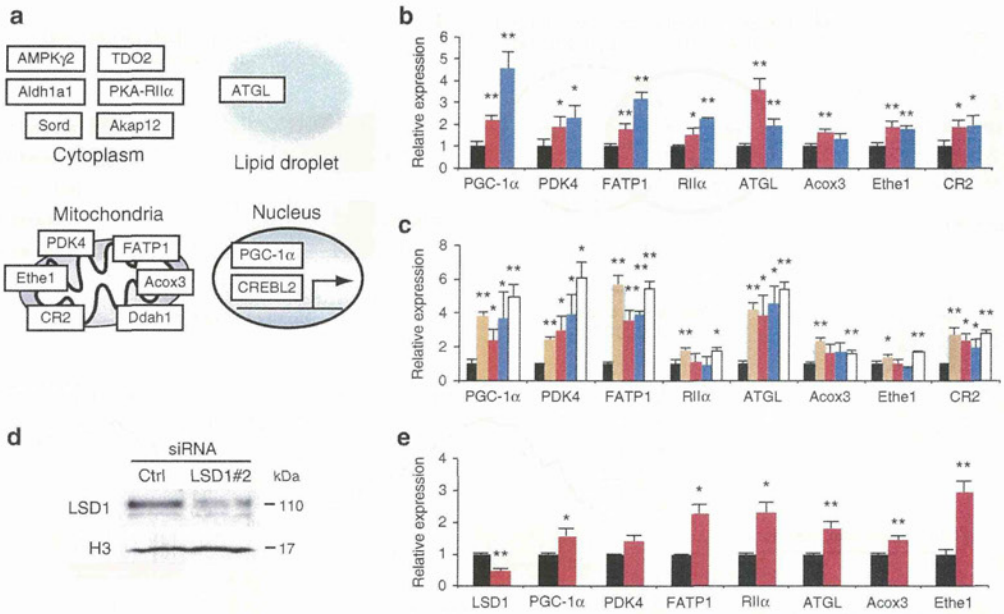

Figure 2 | LSD1 inhibition activates genes for energy expenditure and mitochondrial metabolism in adipocytes. (**a**) Summarized illustration of co-target genes. Co-target genes , associated with energy expenditure and mitochondrial metabolism, are shown with cellular localization of the gene products. (**b**) Expression levels of LSD1 target genes under LSD1-KD (red bars) and BHC80-KD (blue bars). Quantitative RT-PCR values were normalized to the expression levels of the *36B4* gene, and are shown as the fold difference against control siRNA-introduced samples (black bars). (**c**) Expression levels of LSD1 target genes after TC (orange bars) or SLIs (S2101 (red bars), S2107 (blue bars), S2111 (white bars)) treatment. TC and SLIs were used at the concentrations of 10^{-4} M and 10^{-5} M, respectively. Values are shown as the fold difference against vehicle-treated samples (black bars). (**d**) The knockdown of LSD1 using an alternative siRNA (LSD1#2). (**e**) The effect of LSD1 siRNA#2 on the expression of newly identified LSD1-target genes. Values are shown as the fold difference against control siRNA-introduced samples (black bars). All histogram data are means±s.d. of triplicate results. $^{*}P<0.05$, $^{**}P<0.01$ versus control by Student's *t*-test.

We then investigated the mechanism of LSD1-mediated transcriptional repression. LSD1-regulated promoters were enriched with relatively high levels of methylated H3K4, consistent with their active transcription in adipose cells (Fig. 3f). The knockdown of H3K4 methyltransferase Set7/9 resulted in a partial reduction of methylated H3K4, suggesting that methylation equilibrium on these promoters was formed through active methylation/demethylation forces (Fig. 3g). Treatment of the cells with Trichostatin A (TSA), a HDAC inhibitor, induced histone H3 acetylation of the energy-expenditure genes without affecting H3K4 methylation status (Fig. 3h). This suggests that enhanced H3K4 methylation by LSD1 inhibition was not merely a reflection of active chromatin formation, but rather indicates the direct relationship between LSD1 function and H3K4 methylation on these promoters. Typical repressive histone marks, methylated H3K9 and H3K27, were detected only at background levels on LSD1-target promoters, and were not influenced by LSD1-KD (Fig. 3i).

To assess promoter silencing by LSD1, reporter assays were performed in which the mouse *PGC-1α* promoter was fused to the *luciferase* reporter gene (PGC-1α/Luc) (Fig. 4a). As expected, PGC-1α/Luc activity was induced by LSD1-KD and BHC80-KD (Fig. 4b). As well, TC and SLIs significantly activated the *PGC-1α* promoter (Fig. 4c,d). We also examined the chromatin regulation of the PGC-1α/Luc transgene by LSD1. The ChIP assay confirmed that the transfected PGC-1α/Luc plasmid was engaged with histone H3, indicating the incorporation of the transgene into the nucleosome structure (Fig. 4e). TC treatment induced the increase of H3K4 di-methylation at the 5′ region of the transgenic PGC-1α promoter where LSD1 was bound (Fig. 4f,g). Thus, energy-expenditure genes are direct targets of the LSD1-mediated repression.

LSD1 inhibition activates mitochondrial metabolism. As the LSD1 inhibition resulted in the expression of energy-expenditure genes associated with mitochondrial metabolism, we sought to determine the metabolic consequences of LSD1-inhibited conditions. To address this, LSD1-inhibited differentiating 3T3-L1 cells were stained with JC-1, a fluorescent dye that binds to the mitochondrial inner membrane showing green fluorescence (FL1; mitochondrial mass) and forms red-fluorescent aggregates depending on the membrane potential (FL2; respiratory activity)[32]. Flow cytometric analyses of JC-1-stained cells revealed that LSD1-KD significantly augmented the mitochondrial membrane potential with an elevated FL2/FL1 ratio that represents the respiratory activity relative to the mitochondrial surface area (Fig. 5a). TC and SLIs also potently augmented the mitochondrial metabolism although pargyline did not (Fig. 5b; Supplementary Fig. 3a,b). The activated oxidative metabolism by LSD1 inhibition was also confirmed by measuring the OXPHOS capacity using a XF24 Extracellular Flux Analyzer (Seahorse). The maximum OXPHOS capacity was dramatically potentiated by LSD1-KD (Fig. 5c). On the other hand, glycolytic activity, as determined by cellular lactate production, was not significantly affected by either LSD1-KD or TC (Supplementary Fig. S3c,d).

To characterize the metabolic properties of mature adipocytes under LSD1 inhibition, we used an adenovirus-based method to introduce short hairpin RNA (shRNA) into mature 3T3-L1 adipocytes (Supplementary Fig. S4a). LSD1-KD resulted in the significant reduction of lipid accumulation only when the lipogenesis was enhanced under insulin-stimulated condition (Fig. 5d). Consistently, insulin-induced repression of energy-expenditure genes was attenuated by LSD1-KD (Supplementary Fig. 4b). In the insulin-stimulated adipocytes, oxidative metabolism was activated by LSD1-KD and TC treatment (Fig. 5e,f). LSD1 inhibition also reduced

© 2012 Macmillan Publishers Limited. All rights reserved.

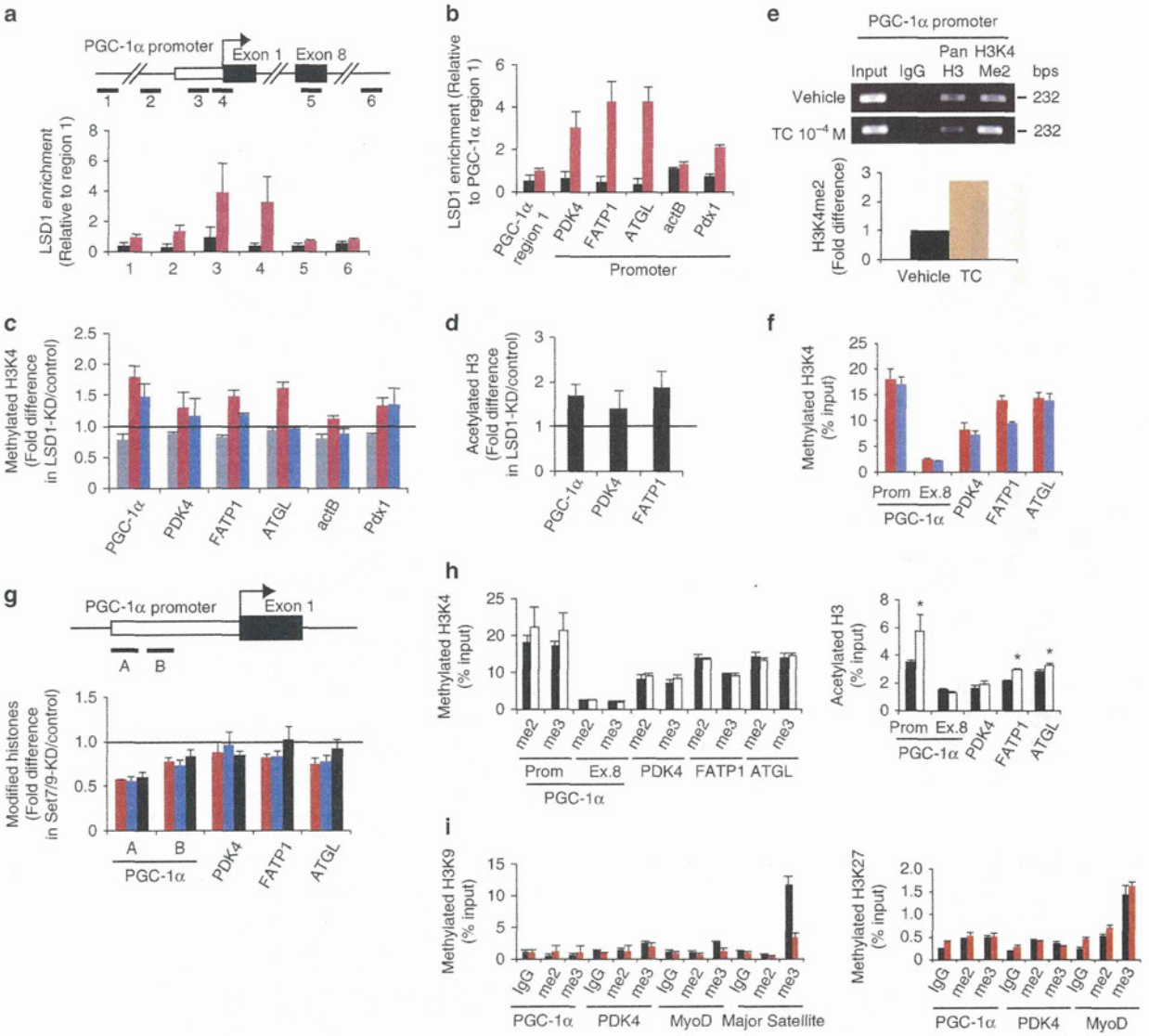

Figure 3 | Epigenetic repression of energy-expenditure genes by LSD1. After 24-hour adipogenic induction, 3T3-L1 cells were examined for LSD1 enrichment and histone modifications by ChIP-qPCR. Before the induction, cells were subjected to siRNA introduction or drug treatment, as specified below. Each ChIP-qPCR histogram indicates the mean±s.d. of triplicate results. (**a**) Localization of LSD1 at the *PGC-1α* gene locus. ChIP analyses were performed in 3T3-L1 cells after 24-hour adipogenic induction using anti-LSD1 antibody. Six indicated sites (1–6) were tested for qPCR amplification. Enrichment values were normalized to input, and shown as the fold difference relative to region 1. Control IgG (black bars), anti-LSD1 antibody (red bars). (**b**) LSD1 occupancy at *PDK4, FATP1 ATGL, actB* and *Pdx1* gene promoters. LSD1 occupancy was calculated as the enrichment level relative to *PGC-1α* gene exon 8. Control IgG (black bars), anti-LSD1 antibody (red bars). (**c**) ChIP analyses of the target gene promoters using antibodies against mono- (grey bars), di- (red bars) and tri-methylated (blue bars) H3K4. The enrichment values are shown as the fold difference relative to control siRNA-introduced cells. (**d**) Histone H3 acetylation levels of LSD1-target promoters after LSD1-KD. (**e**) Enrichment of di-methylated H3K4 at the *PGC-1α* gene promoter in TC-treated cells. Three independent assays had similar results. (**f**) Di- (red bars) and tri-methylation (blue bars) levels of H3K4 on LSD1-regulated genes. Values indicate percentage of input DNA. (**g**) Histone modification levels of LSD1 target promoters after Set7/9-KD. The enrichment values of di- (red bars), tri- (blue bars) methylated H3K4 and acetylated H3 (black bars) are shown as the fold difference relative to control siRNA-introduced cells. (**h**) Effect of TSA treatment on H3K4 methylation (left panel) and H3 acetylation (right panel). Cells were cultured with vehicle (white bars) or with 100 nM TSA (black bars) before adipogenic induction. *$P<0.05$ versus vehicle by Student's *t*-test. (**i**) Repressive histone marks in LSD1-KD (red bars) and control (black bars) cells. ChIP experiments were done using antibodies against di- and tri-methylated H3K9 (left panel) and di- and tri-methylated H3K27 (right panel). *MyoD* gene and major satellite repeat were included as experimental controls.

lipid accumulation in differentiating adipocytes (Supplementary Fig. 4c,d). Thus, LSD1 suppresses mitochondrial energy metabolism in mature adipocytes depending on the cellular energy condition.

Because we observed the activated mitochondrial metabolism and the reduced lipid accumulation in LSD1-inhibited states in adipocytes, we checked whether lipolysis was also activated (Fig. 5g,h). Both LSD1-KD and TC treatment in insulin-stimulated mature 3T3-L1 adipocytes significantly augmented the lipolytic activity. Several types of triglyceride lipases are involved in lipolysis and are mainly controlled by the PKA-mediated signal cascade[24,25].

© 2012 Macmillan Publishers Limited. All rights reserved.

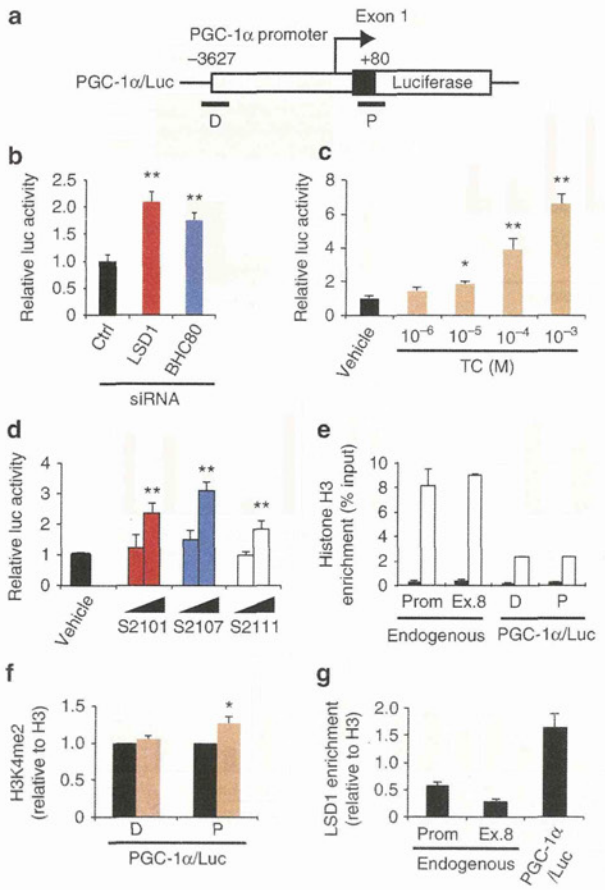

Figure 4 | Transcriptional repression of *PGC-1α* promoter by LSD1. (**a**) Diagram of PGC-1α/Luc construct. Sites of ChIP-qPCR primers are indicated as D (distal) and P (proximal). (**b**) Effects of LSD1-KD and BHC80-KD on *PGC-1α* promoter activity. After the introduction of indicated siRNAs, 3T3-L1 cells were transfected with a PGC-1α/Luc plasmid and an internal control pRL-TK construct. Luciferase activities were measured at 24 h after the adipogenic induction. (**c**,**d**) Effects of LSD1 inhibitors on *PGC-1α* gene promoter activity. TC (**c**) was used at the indicated concentrations whereas SLIs (**d**) were used at 10^{-6} and 10^{-5} M. Reporter-introduced cells were treated with indicated drugs for 24 h before the adipogenic induction. (**e**) Chromatin formation on transfected reporter plasmid. Pan-histone H3 (white bars) and control IgG (black bars) levels were analysed both on endogenous and transgenic *PGC-1α* promoter. (**f**) H3K4 di-methylation level of the reporter vector after vehicle (black bars) or 10^{-4} M TC (orange bars) treatment. Values are normalized to the enrichment level of panH3. (**g**) LSD1-binding on the reporter vector. Values are normalized to the enrichment level of panH3. Values are mean±s.d. of triplicate samples. $^{*}P<0.05$, $^{**}P<0.01$ versus control siRNA or vehicle by Student's *t*-test.

Consistently, *ATGL* and a number of PKA-associated genes were upregulated in LSD1-inhibited cells (Fig. 2a–c; Supplementary Data 1). Collectively, these results suggest that LSD1 suppresses energy expenditure by inhibiting mitochondrial respiration and lipid mobilization in adipocytes.

Loss of FAD attenuates the gene regulatory activity of LSD1. To investigate the biological importance of FAD-dependent LSD1 activities, we examined whether cellular FAD synthesis affects the expression of the LSD1-target genes involved in energy metabolism. The biosynthetic pathway from riboflavin to FAD is composed of two enzymes, riboflavin kinase (RFK) and FAD synthetase (FADS)[33] (Fig. 6a). The siRNA-mediated knockdown of these two genes resulted in a mild reduction of the cellular FAD content in 3T3-L1 cells whereas RFK-KD showing the stronger effect, as assessed by two different methods (Supplementary Fig. S5a,b). Expression of most LSD1-target genes was increased by RFK-KD while FADS-KD did not affect *PGC-1α* expression, in agreement with their effects on FAD production (Fig. 6b; Supplementary Fig. S5c). These results imply that RFK is the rate-limiting enzyme in the FAD biosynthetic process. It might be analogous to the case of the NAD^+ (nicotinamide adenine dinucleotide) synthetic pathway in which Nampt, the first enzyme of the process, strongly affects the cellular NAD^+ pool[34]. To elucidate the substantial overlap in the target genes, expression microarray analysis was performed using LSD1-KD and RFK-KD cells (Fig. 6c). A total of 132 genes were commonly induced more than twofold compared with the control under both knockdown conditions. In addition, as we focused on the probe sets upregulated by LSD1-KD, we found significant enrichment of the probe sets that were similarly upregulated by RFK-KD ($P=3.5\times10^{-47}$ by χ^2 test), compared with those oppositely regulated (Fig. 6d).

Earlier studies have identified the 'GxGxxG' sequence as a FAD-binding consensus, one that is frequently present in FAD-dependent oxidases[35] (Supplementary Fig. S5d). To test whether FAD-binding is required for LSD1-mediated transcriptional repression, we point-mutated The 'GxGxxG' motif located at the amino-terminal side to the catalytic domain of LSD1. Structural modelling of LSD1 predicted that these mutations would deteriorate the LSD1/FAD interaction without affecting the overall folding of the protein[36] (Supplementary Fig. S5e,f). In the GAL4 reporter assay, wild-type LSD1 (GAL4-LSD1wt) suppressed the luciferase activities in a dose-dependent manner, whereas FAD binding-defective LSD1 (GAL4-LSD1mut) did not (Fig. 6e). We then tested whether cellular FAD production directly affects the repressive activity of LSD1. When FAD production was impaired by RFK-KD in 3T3-L1 cells, transcriptional repression by GAL4-LSD1wt was partly abolished (Fig. 6f). We also used lumiflavin, a riboflavin analogue that antagonizes the riboflavin transport into the cells[37], which reduced the cellular FAD content (Supplementary Fig. S5g). LSD1 function was abrogated when lumiflavin was added to the culture medium (Fig. 6g). More importantly, the expression of endogenous LSD1 target genes was elevated after lumiflavin treatment (Fig. 6h). Lumiflavin also caused the reduction of LSD1 protein without affecting the messenger RNA level (Supplementary Fig. S5h), raising the possibility that LSD1 protein might be unstable when it is not bound to FAD. Taken together, these results suggest that LSD1 transcriptionally controls energy metabolism in a cellular FAD-dependent manner.

To address whether the metabolic environment affects LSD1 activities, we examined the cellular FAD levels under the lipogenic conditions in 3T3-L1 cells. Interestingly, cellular FAD content remarkably increased during the adipogenic differentiation (Fig. 6i). In addition, palmitate exposure, which has been shown to facilitate lipid storage and suppress PGC-1α expression[38,39], also led to an increase of FAD content in mature 3T3-L1 adipocytes (Fig. 6j). During the adipogenesis, the expression of LSD1-target genes including PGC-1α, PDK4 and FATP1 were increased, possibly reflecting their importance in adipocyte function (Supplementary Fig. S6a). The elevated FAD level may account for the activation of FAD-demanding processes such as fatty acid oxidation and TCA cycle on adipogenic differentiation. Palmitate exposure slightly reduced the expression levels of these genes, although not statistically significant (Supplementary Fig. S6b). The FAD content in the epididymal WAT from normal-diet (ND)- and high-fat-diet (HFD)-fed mice was measured, but no significant difference was found (Supplementary Fig. S6c). In this experiment, FAD concentration was about ten times lower than that of cultured adipocytes, possibly reflecting the

© 2012 Macmillan Publishers Limited. All rights reserved.

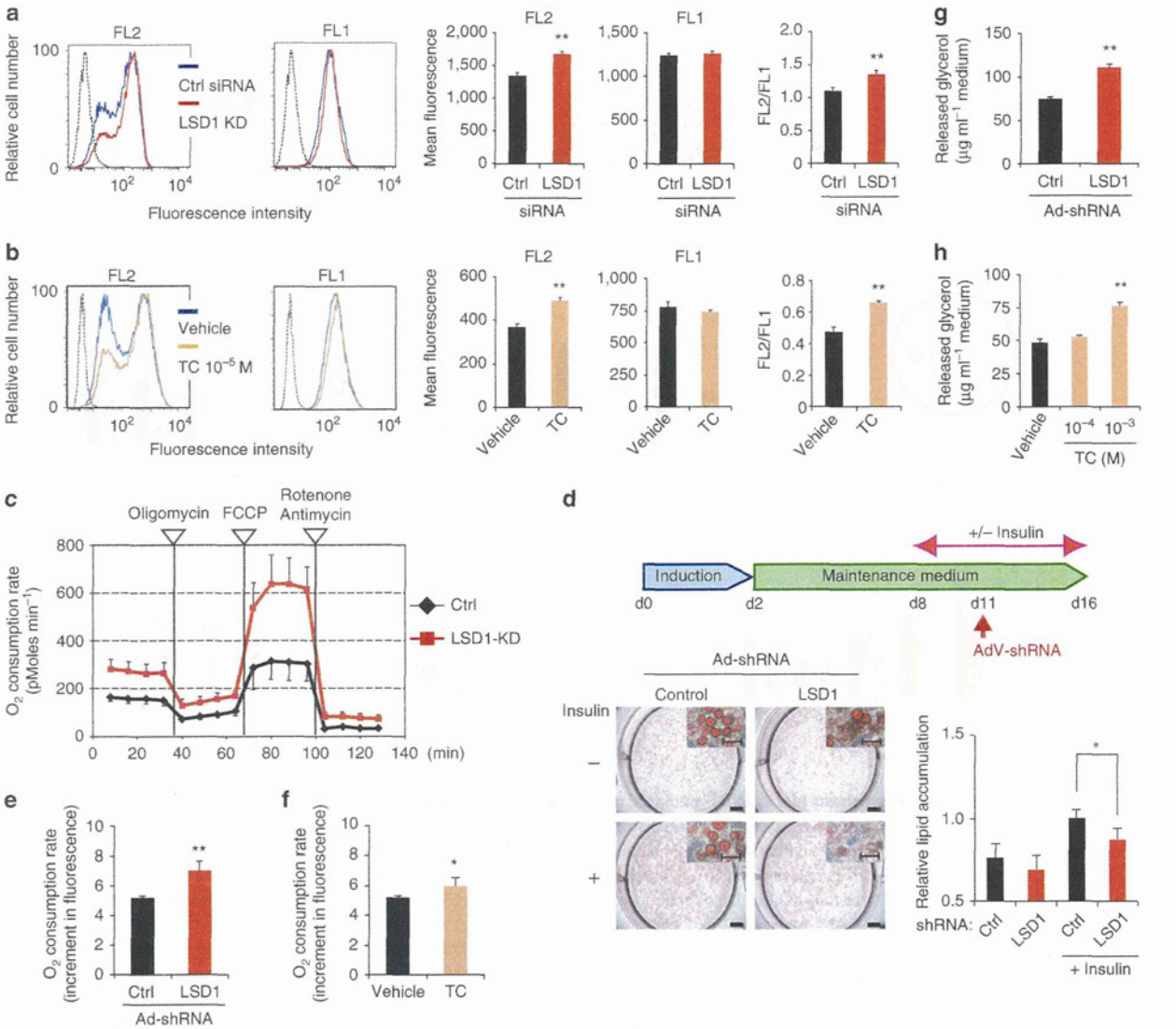

Figure 5 | LSD1 inhibition enhances mitochondrial metabolism in adipocytes. Mitochondrial energy metabolism was assessed in differentiating 3T3-L1 cells under LSD1-KD (**a**) and TC treatment (**b**). siRNA-introduced or drug-treated cells were subjected to adipogenic induction for 24 h, and were stained with JC-1 followed by flow cytometric analyses. Red fluorescent JC-1 aggregates (FL2) and green fluorescent monomers (FL1) were measured. Hatched histograms indicate the unstained control samples. Each histogram shows the representative result of triplicate samples. (**c**) The effect of LSD1-KD on the OXPHOS capacity of differentiating 3T3-L1 cells. OXPHOS activity was determined by measuring the OCR using the XF24 Analyzer. During the real-time measurement, respiratory chain inhibitors were added to the culture at the indicated time points. Values are means±s.d. of five assay wells at each time point. (**d**) LSD1-KD reduces lipid accumulation in insulin-stimulated adipocytes. Differentiated 3T3-L1 cells were cultured in the absence or presence of insulin, followed by adenovirus-mediated introduction of LSD1 shRNA (Ad-shLSD1) or control (Ad-sh-ctrl). Cellular lipid was analysed at 4 days after infection. Values are means±s.d. of five mice. Scale bars in the whole-well and magnified images indicate 5 mm and 50 μm, respectively. (**e**,**f**) The effects of LSD1-KD and TC treatment on the OCR in mature 3T3-L1 adipocytes. Insulin-stimulated adipocytes were treated with shRNA-containing adenoviruses (control or LSD1, **e**) or 10^{-4} M TC (**f**), and cultured for 4 days. OCR was determined using the Oxygen Biosensor System, and was calculated as the fold increase during 30 min-measurement. (**g**,**h**) Enhanced lipolysis in LSD1-inhibited adipocytes. Insulin-stimulated mature 3T3-L1 adipocytes were infected with shRNA-containing adenovirus (**g**) or were treated with TC (**h**), and cultured for 4 days. All values (except for those in **c**) are means±s.d. of three independent samples. $^{*}P<0.05$, $^{**}P<0.01$ versus control siRNA, control shRNA or vehicle by Student's *t*-test

difference in the magnitude of oxidative stress or the instability of FAD in tissue samples. The results show that the FAD content fluctuates depending on the cellular metabolic status, but further study is necessary to elucidate how FAD is utilized in different biological processes in the cell.

Effect of LSD1 inhibition on gene expression in obese WAT. To address the LSD1-dependent metabolic gene regulation *in vivo*, we performed gene-expression analyses in normal and obese adipose tissues of mice. Seven-week old C57BL/6J mice were fed a HFD for six weeks and acquired an obese state. Interestingly, in the adipose tissues of HFD-fed mice, the expression of LSD1 and BHC80 was markedly elevated compared with ND controls (Fig. 7a,b). In addition, the expression of the LSD1 target genes such as *PGC-1α*, *PDK4* and *FATP1* was significantly reduced in the obese WAT tissues (Fig. 7c), indicating an inverse correlation with LSD1/BHC80 expression.

© 2012 Macmillan Publishers Limited. All rights reserved.

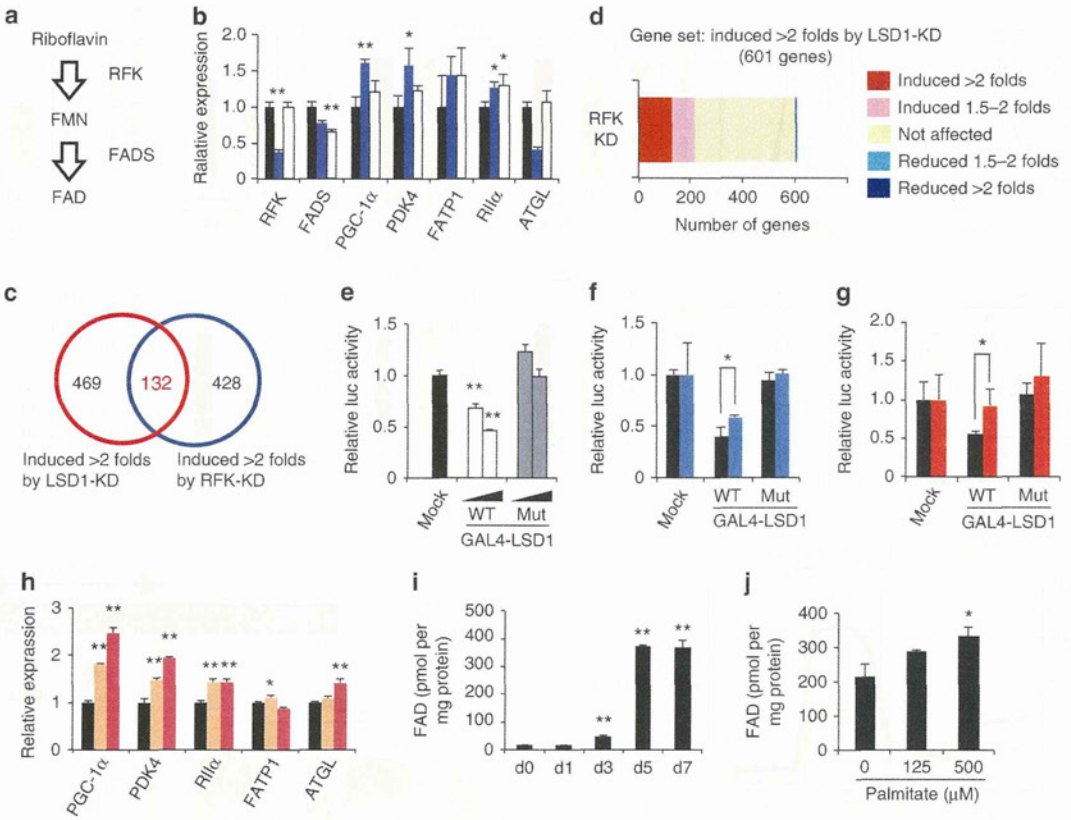

Figure 6 | Inhibition of cellular FAD synthesis blocks LSD1-mediated repression of energy-expenditure genes. (**a**) Biosynthesis pathway of FAD in mammalian cells. Flavin mononucleotide (FMN). (**b**) Effect of the disruption of FAD synthesis on LSD1-target genes. RFK- (blue bars) or FADS- (white bars) knockdown 3T3-L1 cells were induced to differentiate for 24 h, followed by RNA extraction and quantitative RT–PCR. Values are shown as the fold difference against control siRNA-introduced samples (black bars). $^{*}P<0.05$, $^{**}P<0.01$ versus control siRNAs by Student's *t*-test. (**c**) Venn diagram of the probe sets induced by LSD1-KD and RFK-KD. (**d**) Unidirectional effects of RFK-KD on LSD1-target genes. (**e**) Effect of wild-type or FAD-binding mutant-type LSD1 on promoter activity. GAL4-fused LSD1-expressing plasmid (0.1 or 0.5 μg) was transfected into 293T cells, together with the GAL4x5-containing luciferase reporter construct. $^{**}P<0.01$ versus GAL4 mock by Student's *t*-test. (**f**) Effect of RFK-KD on LSD1-mediated transcriptional repression. Control (black bars) or RFK (blue bars) siRNA-introduced 3T3-L1 cells were transfected with indicated GAL4 plasmids 48 h before the luciferase measurement. $^{*}P<0.05$ between indicated conditions by Student's *t*-test. (**g**) Effect of lumiflavin treatment on LSD1-mediated transcriptional repression. 3T3-L1 cells were exposed to vehicle (black bars) or 50 μM lumiflavin (red bars) 48 h before the luciferase measurement. (**h**) Effect of lumiflavin on endogenous LSD1-target genes. Differentiating 3T3-L1 cells were exposed to vehicle (black bars), 25 μM (orange bars) or 50 μM (red bars) lumiflavin for 24 h and were subjected to RNA analyses. (**i**) Increase of FAD concentration during adipogenic differentiation of 3T3-L1 cells. $^{**}P<0.01$ versus day 0 by Student's *t*-test. (**j**) Increase of FAD concentration after 24-hour palmitate exposure in mature 3T3-L1 adipocytes (day 7). Values are normalized to the protein concentration. $^{*}P<0.05$ versus control by Student's *t*-test. All histogram values are means±s.d. of three independent samples.

To verify the direct relationship between LSD1 function and its target gene expression in obese adipose tissues, we employed the *ex vivo* culture of epididymal WAT in combination with adenovirus-mediated depletion of LSD1. We dissected adipose tissues from HFD-fed obese mice, and analysed the metabolic gene expression, 3 days after adenovirus introduction (at a multiplicity of infection (MOI) of 1.5×10^{8} pfu dissected tissues^{-1}) (Fig. 7d). In agreement with the above data, the loss of LSD1 increased the expression of some energy-expenditure genes such as *PGC-1α* and *PDK4* in obese adipose tissues (Fig. 7e). Interestingly, when tissues from ND-fed mice were used, LSD1-KD did not induce energy-expenditure gene expression suggesting the energetic state-dependent action of LSD1 (Fig. 7f). To further characterize the role of LSD1 in obese adipose tissues *in vivo*, we directly introduced the LSD1 shRNAs-expressing adenovirus into epididymal WAT (at a MOI of 5×10^{8} pfu per mouse). Our repeated experiments using adenoviruses carrying the *EGFP* gene or LSD1 shRNAs showed the efficient introduction of exogenous gene into visceral adipose tissues (Fig. 7g). In agreement with the *ex vivo* studies, LSD1-KD *in vivo* induced relatively small but constant activation of the energy-expenditure genes in obese WAT without any evident tissue/cell defects (Fig. 7h). Thus, LSD1 represses energy-expenditure genes in adipose tissues, possibly participating in the establishment of the metabolic phenotypes *in vivo*.

To evaluate the effect of TC administration on diet-induced obesity and the expression of energy-expenditure genes in adipose tissues *in vivo*, C57BL/6J mice were fed a HFD for six weeks in combination with an alternate-day administration of TC (10 mg per kg body weight) (HFD/TC) or PBS (HFD/PBS). HFD/TC mice showed markedly lower body weight and fat mass compared with the HFD/PBS-mice, with an improvement of the systemic lipid handling (Supplementary Fig. S7a–d). There was no difference in food intake among the groups (Supplementary Fig. S7e), and there were no abnormal behaviour or neurological symptoms in the TC-treated mice. Importantly, TC treatment induced the expression of *PGC-1α* and other LSD1 targets as well as BAT marker *UCP-1* in the epididymal WAT of the HFD/TC mice (Supplementary Fig. S7f).

© 2012 Macmillan Publishers Limited. All rights reserved.

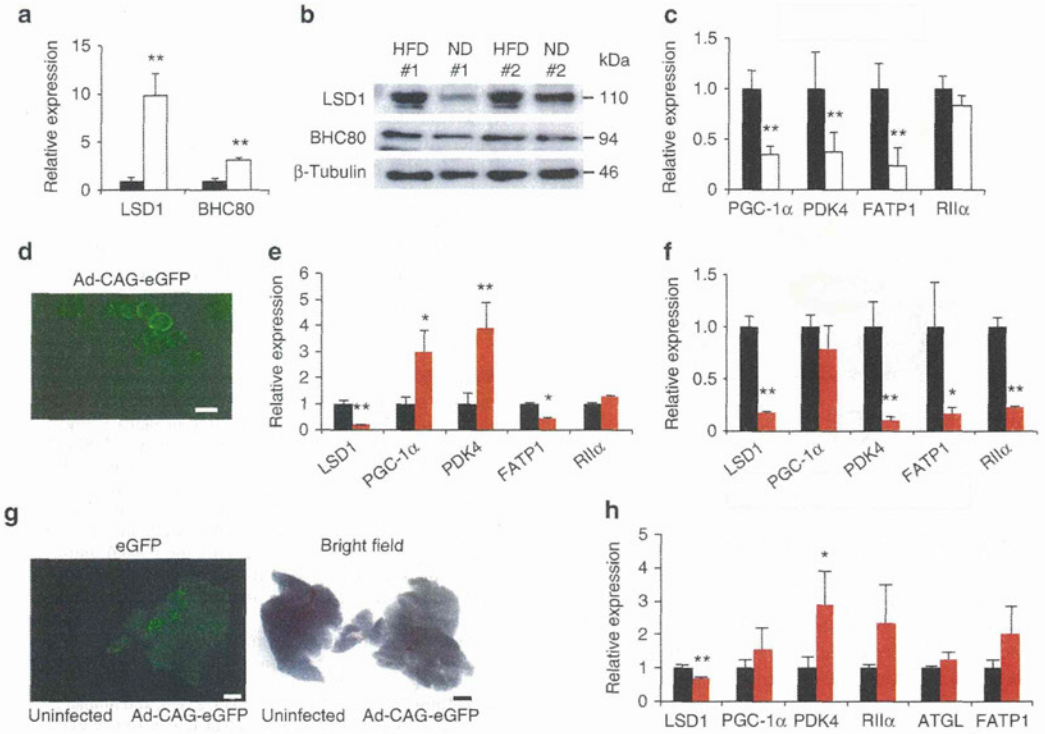

Figure 7 | Inhibition of LSD1 induces energy-expenditure genes in obese adipose tissues. (**a**,**b**) Expression of LSD1 and BHC80 in epididymal WAT from ND (black bars) and HFD- (white bars) fed mice. After a 16-hour fasting period, epididymal WAT was collected, and the total RNA was used for quantitative RT-PCR (**a**). The expression level of the *36B4* gene was used as the internal control. Protein levels are shown by western blot analysis (**b**). (**c**) Expression of LSD1 target genes in ND- (black bars) and HFD- (white bars) fed mice. Values are means±s.d. of four mice, and are shown as fold changes relative to ND-fed mice. $^{**}P<0.01$ versus ND-fed mice by Student's *t*-test. (**d**) Efficient introduction of adenovirus vector into cultured WAT. Adenovirus vector, Ad-CAG-eGFP was introduced into isolated epididymal WAT, and the eGFP expression was analysed by fluorescence microscopy. Scale bar indicates 50 μm. (**e**,**f**) Expression of energy-expenditure genes after adenovirus-mediated knockdown of *LSD1* gene in cultured WAT *ex vivo*. Epididymal WAT was dissected from either HFD- (**e**) or ND-fed mice (**f**), followed by the infection of adenoviruses, Ad-shLSD1 (red bars) or Ad-sh control (black bars). (**g**) Efficient introduction of adenoviral vectors into epididymal WAT *in vivo*. Adenovirus vectors carrying the *eGFP* gene (Ad-CAG-eGFP) was injected into epididymal WAT after incising the outer coat of mice. Four days later, tissues were isolated for the microscopic analysis. Scale bar indicates 2 mm. (**h**) Expression of energy-expenditure genes after adenovirus-mediated reduction of LSD1 in epididymal WAT *in vivo*. Control (black bars) or LSD1 (red bars) shRNA-carrying adenoviruses were directly injected into epididymal WAT of HFD-fed mice 4 days before tissue isolation. Values are means±s.d. of triplicate samples. $^{*}P<0.05$, $^{**}P<0.01$ versus control shRNA by Student's *t*-test.

Collectively, these data further reinforce our finding that LSD1 is involved in the metabolic gene regulation.

Discussion

One of the key factors in formulating an energy strategy is environmental information such as nutritional availability. As many metabolism-associated genes are epigenetically regulated[40], nutrient-driven epigenetic factors may have important roles in forming metabolic phenotypes[3]. LSD1 is a unique demethylase that does not contain the *jumonji* domain but as a flavoenzyme does have the FAD-dependent amine oxidase domain[1]. Our present study clearly indicates that LSD1 negatively regulates energy expenditure that can be reversed by inhibiting LSD1 function and FAD biosynthesis (Fig. 8). Cellular FAD potentiates LSD1 to repress energy-expenditure genes such as *PGC-1α* through H3K4 demethylation in adipocytes where excess energy is stored as triglycerides. Moreover, our experiments using mature adipocytes and isolated adipose tissues revealed the metabolic state-dependent effects of LSD1 inhibition. Thus, the transcriptional and epigenetic regulation by FAD-dependent LSD1 may be central in nutrient-driven metabolic adaptation.

In this study, we identified a set of energy expenditure-associated genes as direct targets of LSD1-mediated repression. We focused on the genes that were commonly induced by LSD1-KD, BHC80-KD and TC treatment. This criterion increased the likelihood of picking up genes that were directly regulated through H3K4 demethylation by LSD1, because BHC80 is reportedly the LSD1 partner required for H3K4 demethylation-dependent repression, and TC irreversibly inhibits the catalytic activity of LSD1 (refs 16,17). This finding was further confirmed by the use of SLIs with minimized nonspecific effects. Our microarray results also revealed the non-overlapping effects of LSD1-KD and BHC80-KD on the genome-wide expression profile. This suggests that in many cases, LSD1 and BHC80 regulate gene expression independently, and that BHC80 is dispensable for LSD1 function other than H3K4 demethylation. In fact, it is reported that BHC80 recognizes H3K4 to facilitate the demethylation by LSD1 (ref. 16), and only a fraction of LSD1 was associated with BHC80 in our experiment (Supplementary Fig. S1c). It is also noteworthy that reported phenotypes of *LSD1*- and *BHC80*-KO mice are distinctively different, indicating the non-overlapping biological function of these genes[11,41].

Mechanistically, LSD1 disruption induced moderate enrichment of methylated H3K4 on actively transcribed promoters. Histone methylation status can be determined by the equilibrium of methylating and demethylating forces, and, in many cases, LSD1 demethylation

© 2012 Macmillan Publishers Limited. All rights reserved.

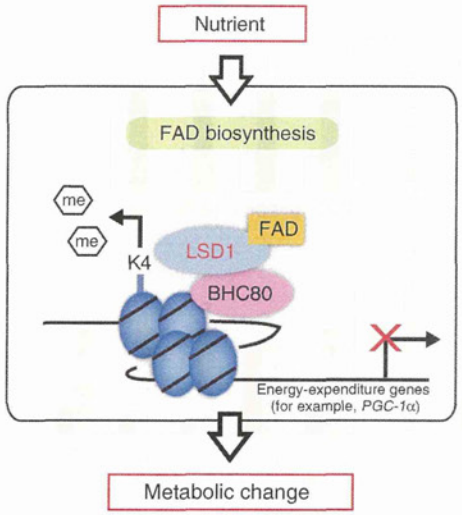

Figure 8 | Schematic model of LSD1 function in the metabolic gene regulation. Schematic model for the epigenetic regulation of energy metabolism by LSD1. FAD-dependent LSD1 facilitates metabolic changes through the repression of energy-expenditure genes via H3K4 demethylation. This pathway may be influenced by nutrients and/or fluctuating FAD level, implicating the link between energetic information and the epigenome.

activity is counteracted by the lysine methyltransferase Set7/9 (refs 9,10). Interestingly, a previous report has shown that glucose-dependent induction of NF-κB gene expression was coincident with Set7/9-dependent H3K4 methylation, and was counteracted by LSD1, implying the possible involvement of Set7/9 in the metabolic gene regulation[42]. In our study, Set7/9-KD resulted in the partial reduction of H3K4 demethylation at LSD1-target promoters (Fig. 3g). Thus, it is possible that LSD1 fine-tunes the expression of metabolic genes so that the cellular energy balance can be properly maintained.

We found in this study that the restriction of cellular FAD availability weakened the LSD1-dependent transcriptional repression of energy-expenditure genes. LSD1, like other flavoenzymes, requires FAD for its catalytic activity and converts it into the reduced form, $FADH_2$ (ref. 43). The catalytic activity of LSD1 may be directly connected to the cellular metabolic state via the fluctuation of the FAD/$FADH_2$ ratio depending on the FAD oxidation processes such as fatty acid β-oxidation and the TCA cycle. Another intriguing possibility is that a physical association between the LSD1 and FAD production machinery determines the LSD1 activities. Indeed, a recent study identified the existence of RFK in the protein complex containing TNFα receptor-1, in which RFK seemed to directly provide NADPH oxidase with FAD, facilitating the TNFα signalling[44]. Such a mechanism might explain why even a small reduction in FAD content in RFK-KD and lumiflavin-treated cells was sufficient for the LSD1 inhibition. In mitochondria, where the majority of FAD production occurs, flavoenzymes may stably associate with FAD even under FAD-reduced conditions[33]. As the FAD reserve for nuclear flavoenzymes is relatively small, their enzymatic activity could be highly sensitive to FAD restriction.

It is of great interest that FAD-dependent LSD1-mediated demethylation may be analogous to, but clearly distinct from, NAD^+-dependent Sirtuin 1 (Sirt1)-mediated deacetylation. Sirt1 is the orthologue of yeast Sir2 histone deacetylase, and promotes mitochondrial activation that contributes to calorie restriction-induced metabolic adaptation[45]. Regarding the regulation of the PGC-1α function, Sirt1 activates PGC-1α protein by deacetylating its lysine residue[46], whereas LSD1 negatively regulates the expression of the *PGC-1α* gene. Such opposing functions of LSD1 and Sirt1 suggest the existence of reciprocal switches for energy homeostasis in which FAD and NAD^+ serve as coenzymatic sensors.

Aberration of cellular energy metabolism is associated with a wide range of multifactor and/or polygenic diseases including obesity-associated diseases, neurological disorders and cancer[47–49]. As epigenetic mechanisms are often linked to the pathogenesis of these diseases, the epigenetic factors responsible would be attractive as pharmacological therapeutic targets[5,50,51]. Our study depicts a novel mechanism of the crosstalk between energy metabolism and epigenetic gene regulation in which the FAD-dependent LSD1 activity regulates energy-expenditure genes. Thus, LSD1 inhibitors may be a new class of epigenetic drugs that can therapeutically benefit a wide range of metabolic disorders.

Methods

Reagents and antibodies. Tranylcypromine hydrochloride, pargyline hydrochloride and lumiflavin were purchased from Sigma. Clorgyline hydrochloride was purchased from MP Biomedicals. The compounds S2101, S2107 and S2111 were synthesized, as previously described[31]. JC-1 was purchased from Molecular Probes. The antibodies used were anti-LSD1 (Abcam, 1:500), anti-mono-methylated histone H3K4 (Abcam, 1:500), anti-di-methylated histone H3K4 (Millipore, 1:500), anti-tri-methylated histone H3K4 (Millipore, 1:500), anti-acetylated histone H3 (Millipore), anti-pan histone H3 (Abcam, 1:2000), anti-di-methylated histone H3K9 (Millipore), anti-tri-methylated histone H3K9 (Millipore), anti-di-methylated histone H3K27 (Millipore), and anti-tri-methylated histone H3K27 (Millipore). Anti-BHC80 antibodies (1:500) were a generous gift from Dr Tadashi Baba (Tsukuba University, Japan)[52]. Antibodies without dilution factors were only used for ChIP experiments. The amount of antibodies used is described here.

Cell culture. Mouse 3T3-L1, C3H10T1/2 cells, and human 293T cells were cultured in DMEM (Sigma) supplemented with 10% (v/v) heat-inactivated fetal bovine serum and penicillin/streptomycin. Adipogenic induction of 3T3-L1 cells was done by a standard method[53]. Post-confluent cells were exposed to adipogenic induction reagents including 0.5 mM 3-isobutyl-1-methylxanthine (Merck), 1 μM dexamethasone (Wako) and 5 μg ml^{-1} insulin (bovine pancreas, Sigma). For the experiments using differentiating adipocytes, cells were collected at 24 h after induction whereas for mature adipocytes, induction medium was replaced with maintenance medium after a 48-h-induction. Lipid accumulation was assessed by oil red O staining. For lipid quantification, oil red O was extracted with 2-propanol and was subjected to colorimetric analysis at 500 nm. For the knockdown experiments, specific siRNAs were introduced to the cells using RNAiMAX reagent (Invitrogen) when they were ~50% confluent. The effective siRNA target sequences are listed in Supplementary Table S3.

Plasmids. To construct pGL3-PGC-1α (PGC-1α/Luc), a luciferase reporter vector containing a mouse *PGC-1α* gene promoter, the fragment (from −3,627 to +80) of this gene was PCR-amplified using primers containing *MluI* and *XhoI* sites at the 5′ and 3′ ends, respectively. The GAL4-DNA-binding domain-fused LSD1 expression vector, pcDNA3-GAL4-hLSD1wt, was generated by inserting the *EcoRI-NotI* fragment from pcDNA3-Flag-HA-hLSD1 (a gift from Dr Tadashi Baba) into the corresponding sites of pcDNA-GAL4mock. pcDNA3-GAL4-hLSD1mut, which expressed the FAD-binding motif-mutated LSD1, was prepared by site-directed mutagenesis. Two glycine-to-alanine mutations were introduced using the primer pair listed in Supplementary Table S4. GAL4-binding motifs-containing reporter vector (pGL3-GALx5-SNRPN) was described previously[54].

Luciferase reporter assay. Luciferase reporter analyses were performed using a dual-luciferase reporter assay system (Promega), according to the manufacturer's protocol. For *PGC-1α* promoter analysis, the pGL3-PGC-1α reporter vector was co-transfected with the reference vector pRL-TK into 3T3-L1 cells, followed by 24-hour adipogenic induction before luciferase measurement. The siRNAs were introduced 24 h before the reporter transfection. For GAL4 reporter assay, pcDNA-GAL4 plasmids were co-transfected with the reporter plasmid pGL3-GALx5-SNRPN and pRL-TK into 293T or 3T3-L1 cells. After 48-h culture, the cells were collected for luciferase measurement. RFK siRNA was introduced 24 h before plasmid transfection, whereas lumiflavin was added to the culture 24 h before the measurement.

Gene-expression analysis. Total RNA from tissues and cells were extracted using Trizol reagents (Invitrogen). Complementary DNAs were produced using SuperScript III reverse transcriptase (Invitrogen). Quantitative RT–PCR was performed by the SYBR green method using Thunderbird reagents (Toyobo) and ABI 7500 Sequence Detector (Applied Biosciences). Primers used in this study are listed in Supplementary Table S4.

Microarray analysis. Genome-wide expression analysis was performed using a GeneChip Mouse Genome Array 430 2 in combination with a GeneChip

© 2012 Macmillan Publishers Limited. All rights reserved.

Hybridization, Wash and Stain Kit (Affymetrix). Microarray data were repeatedly confirmed at Takara Dragon Genomics Center (Ohtsu, Japan). siRNA-introduced and TC-treated 3T3-L1 cells were induced to differentiate for 24 h followed by RNA extraction and a quality check using a Bioanalyzer RNA 6000 Nano Assay (Agilent). Data annotation analysis was performed using GeneSpring GX software (Agilent). Gene set enrichment analysis was performed using GSEA ver. 2.0 software provided by the Broad Institute of MIT and Harvard (http://www.broadinstitute.org/gsea/). The accession number of the microarray data in GEO is GSE18600.

Chromatin immunoprecipitation and co-IP. In the ChIP experiments for detecting modified histones, cells were crosslinked with 1% formaldehyde[55]. Following the cell lysis, isolated nuclei were subjected to sonication for chromatin fragmentation. Chromatin fragments were incubated at 4 °C overnight with appropriate antibodies, followed by a pull-down assay using protein A/G-conjugated agarose beads. Purified DNAs were subjected to quantitative PCR (qPCR) using the primer sets listed in Supplementary Table S4. To detect LSD1 enrichment on the genomic DNAs, we employed a protocol for detecting indirect associations between protein and DNA[56]. Briefly, enhanced crosslinking of chromatin using formaldehyde and protein-protein chemical crosslinker DTBP (dimethyl 3, 3′-dithiobispropionimidate 2HCl) (Sigma) was performed to increase the stability of protein-DNA complexes. Chromatin fragmentation was done by sonication in a regular RIPA buffer containing 0.1% SDS, followed by immunoprecipitation, as described above. For co-IP experiments, cells were lysed in IP buffer (50 mM Tris–HCl pH 8.0, 5 mM EDTA 150 mM NaCl, 0.5% NP-40, 0.5% Triton-X100) and incubated with specific antibodies followed by the pull-down with protein A-sepharose beads for subsequent western blot analyses.

Generation of adenoviral vectors that express shRNA. The 65-bp oligonucleotides containing specific shRNA for LSD1 (5′-GATCCCACAAGGAAAGCTA GAAGATTCAAGAGATCTTCTAGCTTTCCTTGTGTTTTTTACGCGTG-3′; the target sequence is underlined), BHC80 (5′-GATCCGTTCCAGATACAGCCATT GTTCAAGAGACAATGGCTGTATCTGGAACTTTTTTACGCGTG-3′) and control GL3 (5′-GATCCGATTTCGAGTCGTCTTAATTTCAAGAGAATTAAGAC GACTCGAAATCTTTTTTACGCGTG-3′) (synthesized by TaKaRa Bio Company) were ligated to the BamHI and EcoRI sites of RNAi-Ready pSIREN-Shuttle Vector (Clontech Laboratories). and were subsequently sequenced for verification. The DNA fragment containing LSD1, BHC80 or GL3-specific shRNA downstream to the human U6 promoter was subcloned into adenoviral vector plasmid pAd.HM4, and was transfected to 293 cells. The generated replication-deficient adenoviral vector was propagated, purified and tittered, as described previously[57,58].

Expression of shRNA in isolated adipose tissues. For *ex vivo* adipose tissue culture, epididymal WAT of mice was obtained, dissected into ~3-mm cubes and maintained in primary culture medium (DMEM/F12 (1:1) supplemented with 10% FBS, 100 μM ascorbic acid, 100 nM insulin and 200 pM 3, 3′, 5-triiodo L-thyronine). For adenovirus infection, three tissue blocks were placed into a single well of 48-well plate and exposed to adenovirus expressing either control or LSD1 shRNA at a MOI of 1.5×10^8 plaque-forming units (pfu) per well. Infections were repeated in triplicate wells for each virus.

***In vivo* introduction of adenoviruses**. We used adenovirus transiently expressing LSD1 shRNAs in WAT *in vivo*, because LSD1-deficient mice and cells had severe defects[11]. For *in vivo* LSD1-knockdown experiments, adenoviruses were directly injected into the epididymal WAT of HFD-fed mice. Under anaesthesia, the outer coats of mice were dissected at the lower part of the abdomen. In obese mice, a portion of epididymal WAT was visible through the peritoneum, enabling targeted injection of adenoviruses. Adenoviruses expressing either control or LSD1 shRNAs were injected into the epididymal WAT on the right side of the abdomen at a MOI of 5×10^8 pfu per mouse. Four days after injection, tissues were collected for RNA analyses.

Assessment of cellular metabolism. For the determination of mitochondrial metabolism, 3T3-L1 cells were stained with fluorescence dye JC-1, followed by flow cytometric analysis[32]. Following trypsinization, cells were exposed to 5 μg ml^{-1} of JC-1 in the culture medium for 15 min at 37 °C and were suspended in PBS for fluorescence-activated cell sorting (FACS) analysis. Green and red fluorescent signals detected mitochondrial mass (FL1) and mitochondrial membrane potential (FL2), respectively, using a FACS Canto cytometer (Becton Dickinson). Cellular lipolytic activity was determined by measuring the concentration of free glycerol released into the culture medium during the 24-h culture, using an Adipolysis Assay Kit (Cayman Chemical). Cellular lactate content was measured using a Lactate Assay Kit II (BioVision), according to the manufacturer's instructions. Oxygen consumption was measured using a BD Oxygen Biosensor (BD Falcon), according to the manufacturer's instructions. For the assay, adipocytes were dispersed into single cells by Accumax reagent (Innovative Cell Technologies) and resuspended in the culture medium. Cell numbers were calculated for the normalization of the oxygen consumption values. Oxygen consumption rate (OCR) values were calculated as the fold-increase during a 30-min-measurement.

Real-time measurement of OXPHOS activity. Real-time monitoring of cellular OXPHOS activity was performed using XF24 Extracellular Flux Analyzer (Seahorse Bioscience), according to the manufacturer's instructions. siRNA-introduced 3T3-L1 cells were inoculated on the assay culture plate and allowed to differentiate for 24 h before the assay. Maximum OXPHOS capacity was determined as previously reported with some modifications[59]. In brief, during the real-time measurement, inhibitors of respiratory chain components were serially added to the culture. First, the complex V inhibitor, oligomycin (1 μg ml^{-1}), was added followed by the addition of the respiratory uncoupler, carbonyl cyanide-*p*-trifluoromethoxyphenylhydrazone (FCCP) (1 μM), and then the complex I and III inhibitors, rotenone (100 nM) and antimycin A (10 μM). After each drug addition, the OCR was measured four times. The addition of FCCP accelerates oxygen consumption to a maximum level, whereas complex I inhibitors completely abolish the mitochondrial respiration. Thus, the difference in OCR between FCCP- and rotenone/antimycin-added states indicates the maximum OXPHOS capacity.

Statistical analyses. Data are presented as means ± s.d. All statistical analyses were performed by a two-tailed Student's *t*-test, except in the microarray experiments, in which Pearson's χ^2 test was carried out.

References

1. Cloos, P. A., Christensen, J., Agger, K. & Helin, K. Erasing the methyl mark: histone demethylases at the center of cellular differentiation and disease. *Genes Dev.* **22,** 1115–1140 (2008).
2. Felsenfeld, G. & Groudine, M. Controlling the double helix. *Nature* **421,** 448–453 (2003).
3. Teperino, R., Schoonjans, K. & Auwerx, J. Histone methyl transferases and demethylases; can they link metabolism and transcription? *Cell Metab.* **12,** 321–327 (2010).
4. Gluckman, P. D. & Hanson, M. A. The developmental origins of the metabolic syndrome. *Trends Endocrinol. Metab.* **15,** 183–187 (2004).
5. Gallou-Kabani, C. & Junien, C. Nutritional epigenomics of metabolic syndrome: new perspective against the epidemic. *Diabetes* **54,** 1899–1906 (2005).
6. Shi, Y. *et al.* Histone demethylation mediated by the nuclear amine oxidase homolog LSD1. *Cell* **119,** 941–953 (2004).
7. Metzger, E. *et al.* LSD1 demethylates repressive histone marks to promote androgen-receptor-dependent transcription. *Nature* **437,** 436–439 (2005).
8. Huang, J. *et al.* p53 is regulated by the lysine demethylase LSD1. *Nature* **449,** 105–108 (2007).
9. Yang, J. *et al.* Reversible methylation of promoter-bound STAT3 by histone-modifying enzymes. *Proc. Natl Acad. Sci. USA* **107,** 21499–21504 (2010).
10. Wang, J. *et al.* The lysine demethylase LSD1 (KDM1) is required for maintenance of global DNA methylation. *Nat. Genet.* **41,** 125–129 (2009).
11. Wang, J. *et al.* Opposing LSD1 complexes function in developmental gene activation and repression programmes. *Nature* **446,** 882–887 (2007).
12. Forneris, F., Binda, C., Vanoni, M. A., Mattevi, A. & Battaglioli, E. Histone demethylation catalysed by LSD1 is a flavin-dependent oxidative process. *FEBS Lett.* **579,** 2203–2207 (2005).
13. Bugg, T. D. H. *Introduction to Enzyme & Coenzyme Chemistry* 2nd edn (Blackwell Publishing, 2004).
14. Modjtahedi, N., Giordanetto, F., Madeo, F. & Kroemer, G. Apoptosis-inducing factor: vital and lethal. *Trends Cell Biol.* **16,** 264–272 (2006).
15. Pospisilik, J. A. *et al.* Targeted deletion of AIF decreases mitochondrial oxidative phosphorylation and protects from obesity and diabetes. *Cell* **131,** 476–491 (2007).
16. Lan, F. *et al.* Recognition of unmethylated histone H3 lysine 4 links BHC80 to LSD1-mediated gene repression. *Nature* **448,** 718–722 (2007).
17. Lee, M. G., Wynder, C., Schmidt, D. M., McCafferty, D. G. & Shiekhattar, R. Histone H3 lysine 4 demethylation is a target of nonselective antidepressive medications. *Chem. Biol.* **13,** 563–567 (2006).
18. Schmidt, D. M. & McCafferty, D. G. trans-2-Phenylcyclopropylamine is a mechanism-based inactivator of the histone demethylase LSD1. *Biochemistry* **46,** 4408–4416 (2007).
19. Gatta, R. & Mantovani, R. NF-Y substitutes H2A-H2B on active cell-cycle promoters: recruitment of CoREST-KDM1 and fine-tuning of H3 methylations. *Nucleic Acids Res,* **36,** 6592–6607 (2008).
20. Zhu, Q. *et al.* Lysine-specific demethylase 1 (LSD1) Is required for the transcriptional repression of the telomerase reverse transcriptase (hTERT) gene. *PLoS One* **3,** e1446 (2008).
21. Jie, Z. *et al.* Trans-2-phenylcyclopropylamine induces nerve cells apoptosis in zebrafish mediated by depression of LSD1 activity. *Brain Res. Bull.* **80,** 79–84 (2009).
22. Youdim, M. B., Edmondson, D. & Tipton, K. F. The therapeutic potential of monoamine oxidase inhibitors. *Nat. Rev. Neurosci.* **7,** 295–309 (2006).
23. Subramanian, A. *et al.* Gene set enrichment analysis: a knowledge-based approach for interpreting genome-wide expression profiles. *Proc. Natl Acad. Sci. USA* **102,** 15545–15550 (2005).

© 2012 Macmillan Publishers Limited. All rights reserved.

24. Zimmermann, R., Lass, A., Haemmerle, G. & Zechner, R. Fate of fat: the role of adipose triglyceride lipase in lipolysis. *Biochim. Biophys. Acta* **1791,** 494–500 (2009).
25. Holm, C. Molecular mechanisms regulating hormone-sensitive lipase and lipolysis. *Biochem. Soc. Trans.* **31,** 1120–1124 (2003).
26. Sugden, M. C., Bulmer, K. & Holness, M. J. Fuel-sensing mechanisms integrating lipid and carbohydrate utilization. *Biochem. Soc. Trans.* **29,** 272–278 (2001).
27. Puigserver, P. & Spiegelman, B. M. Peroxisome proliferator-activated receptor-gamma coactivator 1 alpha (PGC-1 alpha): transcriptional coactivator and metabolic regulator. *Endocr. Rev.* **24,** 78–90 (2003).
28. Gesta, S., Tseng, Y. H. & Kahn, C. R. Developmental origin of fat: tracking obesity to its source. *Cell* **131,** 242–256 (2007).
29. Wu, Q. *et al.* Fatty acid transport protein 1 is required for nonshivering thermogenesis in brown adipose tissue. *Diabetes* **55,** 3229–3237 (2006).
30. Sebastian, D. *et al.* Novel role of FATP1 in mitochondrial fatty acid oxidation in skeletal muscle cells. *J. Lipid Res.* **50,** 1789–1799 (2009).
31. Mimasu, S. *et al.* Structurally designed trans-2-phenylcyclopropylamine derivatives potently inhibit histone demethylase LSD1/KDM1. *Biochemistry* **49,** 6494–6503 (2010).
32. Lopez-Lluch, G. *et al.* Calorie restriction induces mitochondrial biogenesis and bioenergetic efficiency. *Proc. Natl Acad. Sci. USA* **103,** 1768–1773 (2006).
33. Barile, M., Brizio, C., Valenti, D., De Virgilio, C. & Passarella, S. The riboflavin/FAD cycle in rat liver mitochondria. *Eur. J. Biochem.* **267,** 4888–4900 (2000).
34. Fulco, M. *et al.* Glucose restriction inhibits skeletal myoblast differentiation by activating SIRT1 through AMPK-mediated regulation of Nampt. *Dev. Cell.* **14,** 661–673 (2008).
35. Kubo, A., Itoh, S., Itoh, K. & Kamataki, T. Determination of FAD-binding domain in flavin-containing monooxygenase 1 (FMO1). *Arch. Biochem. Biophys.* **345,** 271–277 (1997).
36. Mimasu, S., Sengoku, T., Fukuzawa, S., Umehara, T. & Yokoyama, S. Crystal structure of histone demethylase LSD1 and tranylcypromine at 2.25 A. *Biochem. Biophys. Res. Commun.* **366,** 15–22 (2008).
37. Bafunno, V. *et al.* Riboflavin uptake and FAD synthesis in Saccharomyces cerevisiae mitochondria: involvement of the Flx1p carrier in FAD export. *J. Biol. Chem.* **279,** 95–102 (2004).
38. Crunkhorn, S. *et al.* Peroxisome proliferator activator receptor gamma coactivator-1 expression is reduced in obesity: potential pathogenic role of saturated fatty acids and p38 mitogen-activated protein kinase activation. *J. Biol. Chem.* **282,** 15439–15450 (2007).
39. Takahashi, K. *et al.* JNK- and IkappaB-dependent pathways regulate MCP-1 but not adiponectin release from artificially hypertrophied 3T3-L1 adipocytes preloaded with palmitate *in vitro*. *Am. J. Physiol. Endocrinol. Metab.* **294,** E898–909 (2008).
40. Gluckman, P. D., Hanson, M. A., Buklijas, T., Low, F. M. & Beedle, A. S. Epigenetic mechanisms that underpin metabolic and cardiovascular diseases. *Nat. Rev. Endocrinol.* **5,** 401–408 (2009).
41. Iwase, S. *et al.* A component of BRAF-HDAC complex, BHC80, is required for neonatal survival in mice. *FEBS Lett.* **580,** 3129–3135 (2006).
42. Brasacchio, D. *et al.* Hyperglycemia induces a dynamic cooperativity of histone methylase and demethylase enzymes associated with gene-activating epigenetic marks that coexist on the lysine tail. *Diabetes* **58,** 1229–1236 (2009).
43. Anand, R. & Marmorstein, R. Structure and mechanism of lysine-specific demethylase enzymes. *J. Biol. Chem.* **282,** 35425–35429 (2007).
44. Yazdanpanah, B. *et al.* Riboflavin kinase couples TNF receptor 1 to NADPH oxidase. *Nature* **460,** 1159–1163 (2009).
45. Lavu, S., Boss, O., Elliott, P. J. & Lambert, P. D. Sirtuins—novel therapeutic targets to treat age-associated diseases. *Nat. Rev. Drug Discov.* **7,** 841–853 (2008).
46. Rodgers, J. T. *et al.* Nutrient control of glucose homeostasis through a complex of PGC-1alpha and SIRT1. *Nature* **434,** 113–118 (2005).
47. Symonds, M. E., Sebert, S. P., Hyatt, M. A. & Budge, H. Nutritional programming of the metabolic syndrome. *Nat. Rev. Endocrinol.* **5,** 604–610 (2009).
48. Knott, A. B., Perkins, G., Schwarzenbacher, R. & Bossy-Wetzel, E. Mitochondrial fragmentation in neurodegeneration. *Nat. Rev. Neurosci.* **9,** 505–518 (2008).
49. DeBerardinis, R. J., Lum, J. J., Hatzivassiliou, G. & Thompson, C. B. The biology of cancer: metabolic reprogramming fuels cell growth and proliferation. *Cell Metab.* **7,** 11–20 (2008).
50. Urdinguio, R. G., Sanchez-Mut, J. V. & Esteller, M. Epigenetic mechanisms in neurological diseases: genes, syndromes, and therapies. *Lancet Neurol.* **8,** 1056–1072 (2009).
51. Kelly, T. K., De Carvalho, D. D. & Jones, P. A. Epigenetic modifications as therapeutic targets. *Nat. Biotechnol.* **28,** 1069–1078 (2010).
52. Iwase, S. *et al.* Characterization of BHC80 in BRAF-HDAC complex, involved in neuron-specific gene repression. *Biochem. Biophys. Res. Commun.* **322,** 601–608 (2004).
53. Okazaki, H. *et al.* Lipolysis in the absence of hormone-sensitive lipase: evidence for a common mechanism regulating distinct lipases. *Diabetes* **51,** 3368–3375 (2002).
54. Fujita, N. *et al.* Mechanism of transcriptional regulation by methyl-CpG binding protein MBD1. *Mol. Cell. Biol.* **20,** 5107–5118 (2000).
55. Ye, S. K. *et al.* The IL-7 receptor controls the accessibility of the TCRgamma locus by Stat5 and histone acetylation. *Immunity* **15,** 813–823 (2001).
56. Fujita, N. *et al.* Methyl-CpG binding domain 1 (MBD1) interacts with the Suv39h1-HP1 heterochromatic complex for DNA methylation-based transcriptional repression. *J. Biol. Chem.* **278,** 24132–24138 (2003).
57. Takahashi, T. *et al.* Identification and isolation of embryonic stem cell-derived target cells by adenoviral conditional targeting. *Mol. Ther.* **14,** 673–683 (2006).
58. Nagano, S., Oshika, H., Fujiwara, H., Komiya, S. & Kosai, K. An efficient construction of conditionally replicating adenoviruses that target tumor cells with multiple factors. *Gene Ther.* **12,** 1385–93 (2005).
59. Hill, B. G., Dranka, B. P., Zou, L., Chatham, J. C. & Darley-Usmar, V. M. Importance of the bioenergetic reserve capacity in response to cardiomyocyte stress induced by 4-hydroxynonenal. *Biochem. J.* **424,** 99–107 (2009).

Acknowledgements

We are grateful to Dr. Tadashi Baba (Tsukuba University, Japan) for kindly providing the plasmids and an antibody. We thank Drs Tatsuya Kondo, Eiichi Araki and Ryuichi Nishinakamura, and Ms. Sayoko Fujimura (Kumamoto University, Japan), and the members of our laboratory for helpful discussions. This work was supported by a Grant-in-Aid for Scientific Research on Priority Areas from the Ministry of Education, Culture, Sports, Science and Technology (M.N. and S.H.), by a Grant-in-Aid for the Global Center of Excellence (COE) 'Cell Fate Regulation Research and Education Unit', Kumamoto University, and by a grant from the Takeda Science Foundation (M.N.).

Author contributions

S.H. and M.N. designed and performed the experiments, together with supports by A.S., K.N. and K.A. Y.W. and K.K. constructed adenovirus vectors. S.M., T.U. and S.Y. synthesized and analysed the small chemicals. S.H., T.U. and M.N. prepared the manuscript.

Additional information

Accession codes: The microarray data have been deposited in the GEO database under accession code GSE18600.

Supplementary Information accompanies this paper at http://www.nature.com/naturecommunications

Competing financial interests: The authors declare no competing financial interests.

Reprints and permission information is available online at http://npg.nature.com/reprintsandpermissions/

How to cite this article: Hino, S. *et al.* FAD-dependent lysine-specific demethylase-1 regulates cellular energy expenditure. *Nat. Commun.* 3:758 doi: 10.1038/ncomms1755 (2012).

License: This work is licensed under a Creative Commons Attribution-NonCommercial-Share Alike 3.0 Unported License. To view a copy of this license, visit http://creativecommons.org/licenses/by-nc-sa/3.0/

© 2012 Macmillan Publishers Limited. All rights reserved.

Tanaka et al. Diagnostic Pathology 2012, 7:108
http://www.diagnosticpathology.org/content/7/1/108

DIAGNOSTIC PATHOLOGY

CASE REPORT Open Access

Pathological femoral fractures due to osteomalacia associated with adefovir dipivoxil treatment for hepatitis B: a case report

Motoyuki Tanaka[1], Takao Setoguchi[2*], Yasuhiro Ishidou[3], Yoshiya Arishima[1], Masataka Hirotsu[1], Yoshinobu Saitoh[1], Shunsuke Nakamura[1], Hironori Kakoi[1], Satoshi Nagano[1], Masahiro Yokouchi[1], Junichi Kamizono[1] and Setsuro Komiya[1]

Abstract

We present a case of a 62-year-old man who underwent total hip arthroplasty for treatment of pathologic femoral neck fracture associated with adefovir dipivoxil-induced osteomalacia. He had a 13-month history of bone pain involving his shoulders, hips, and knee. He received adefovir dipivoxil for treatment of lamivudine-resistant hepatitis B virus infection for 5 years before the occurrence of femoral neck fracture. Orthopedic surgeons should be aware of osteomalacia and pathological hip fracture caused by drug-induced renal dysfunction, which results in Fanconi's syndrome.

Virtual slides: The virtual slide(s) for this article can be found here: http://www.diagnosticpathology.diagnomx.eu/vs/1600344696739249

Keywords: Osteomalacia, Pathological femoral neck fracture, Adefovir dipivoxil, Hepatitis B, Fanconi's syndrome

Background

Hypophosphatemic osteomalacia caused by proximal renal tubule dysfunction induces Fanconi's syndrome, which leads to impaired reabsorption of amino acids, glucose, urate, and phosphate [1]. The chronic loss of phosphate and impaired synthesis of 1,25-dihydroxyvitamin D3 may lead to failure of bone mineralization. Recently, osteomalacia was reported in cases in which hepatitis B virus and human immunodeficiency virus (HIV) infections were treated using high-dose adefovir dipivoxil [2-6]. We report a case of a patient who underwent total hip arthroplasty for pathological femoral neck fracture associated with osteomalacia induced by low-dose adefovir dipivoxil treatment.

Case presentation

A 62-year-old man started experiencing pain in the right knee and left shoulder pain in January 2010. He visited a clinic and was administered salazosulfapyridine and methylprednisolone therapy for rheumatoid arthritis. However, the pain gradually increased, and he started experiencing pain in his hip joints as well. Therefore, he was admitted our hospital for further examination in February 2011. He had a 7-year history of chronic hepatitis caused by hepatitis B virus infection, and had received lamivudine therapy for 2 years. Because the virus developed resistance to lamivudine, he received adefovir dipivoxil for 5 years before the development of the femoral neck fracture. After adefovir dipivoxil treatment, his liver function was restored. Radiography showed femoral neck fractures (right, Garden III fracture; left, Garden IV fracture) and a distal right tibial fracture (Figure 1a) [7]. Magnetic resonance imaging (MRI) of both hip joints showed fractures across the right and left femoral neck and bone edema, which had low intensity on T1-weighted images and high intensity on T2-weighted images (Figure 1b). ^{99m}Tc-hydroxymethylene diphosphonate (HMDP) whole-body bone scintigraphy showed increased uptake of the radiotracer in the calvaria, maxilla, both scapulae, ribs, both femoral necks, right condyle of the femur, right tibia, and both tarsi (Figure 1c). He showed hypophosphatemia

* Correspondence: setoro@m2.kufm.kagoshima-u.ac.jp
[2]The Near-Future Locomotor Organ Medicine Creation Course (Kusunoki Kai), Graduate School of Medical and Dental Sciences, Kagoshima University, 8-35-1 Sakuragaoka, Kagoshima 890-8520, Japan
Full list of author information is available at the end of the article

BioMed Central

© 2012 Tanaka et al.; licensee BioMed Central Ltd. This is an Open Access article distributed under the terms of the Creative Commons Attribution License (http://creativecommons.org/licenses/by/2.0), which permits unrestricted use, distribution, and reproduction in any medium, provided the original work is properly cited.

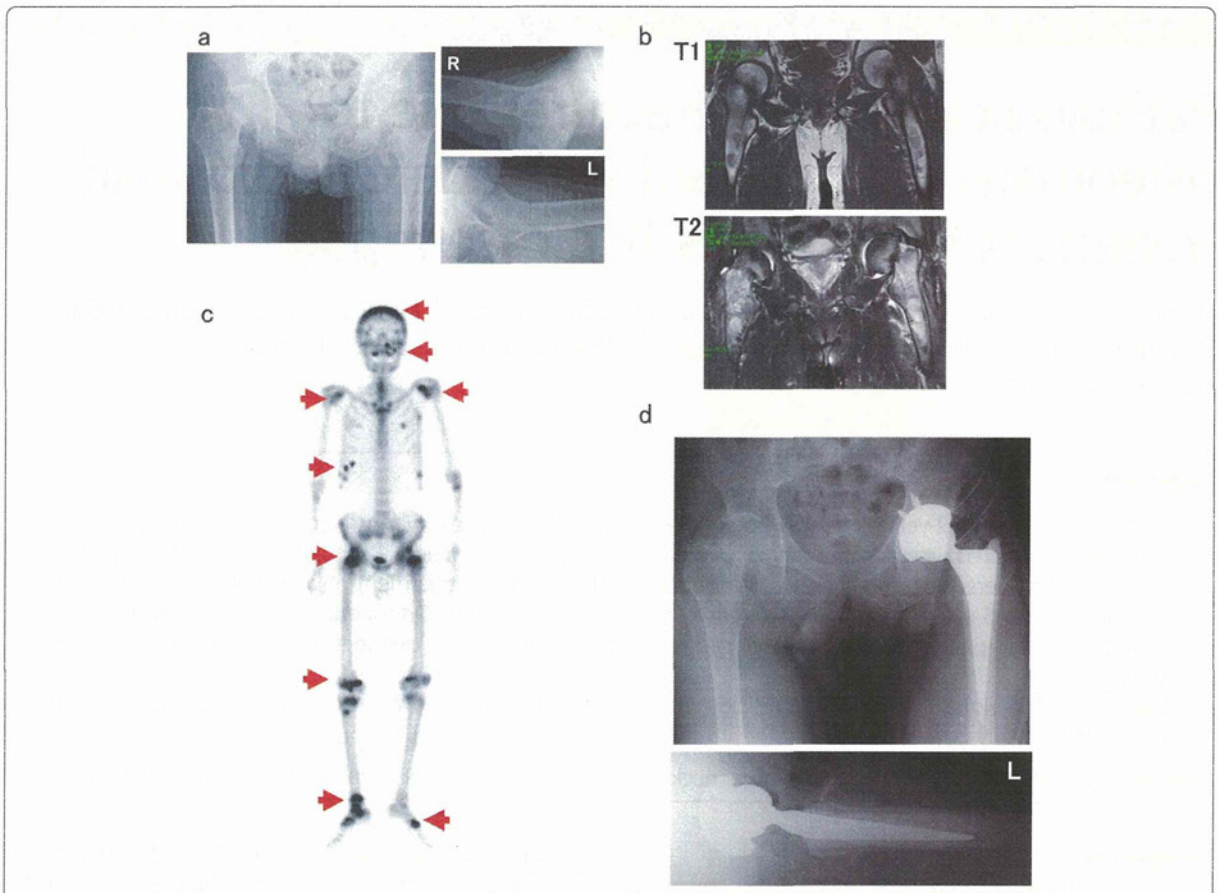

Figure 1 Imaging studies. a: Plain radiographs of both femurs reveal femoral neck fractures. (right, Garden III fracture; left, Garden IV fracture) **b**: Coronal T1-weighted image demonstrates low-intensity femoral neck fractures and the T2-weighted image shows high-intensity bone edema. **c**: ^{99m}Tc-hydroxymethylene diphosphonate (HMDP) scintigraphy demonstrates significant abnormal uptake in calvaria, maxilla, both scapulae, ribs, both femoral necks, right condyle of the femur, right tibia, and both tarsi. **d**: Plain radiographs of hip joints in which total hip arthroplasty was performed by inserting an implant in the left hip joint.

(2.0 mg/dL; normal range, 2.5–4.5 mg/dL) and increased levels of alkaline phosphatase (ALP, 1594 IU/L; normal range, 115–359 IU/L). Furthermore, he showed normal serum creatinine (0.7 mg/dL; normal range, 0.4–0.7 mg/dL), blood urea nitrogen (BUN, 12.3 mg/dL; normal range, 8.0–22.0 mg/dL), intact parathyroid hormone (PTH, 19 pg/mL; normal range, 10–65 pg/mL), and 1,25-dihydroxyvitamin D3 (40.0 pg/mL; normal range, 20–60 pg/mL) levels. Urinalysis revealed proteinuria. A 24-h study showed increased urinary excretion of phosphate (1004 mg/day; normal range, 70–220 mg/day), calcium (471.0 mg/day; normal range, 100–300 mg/day), *N*-acetylglucosaminidase (11.8 U/L; normal range, <7.0 U/L), and β2-microglobulin (64,579 μg/L; normal range, 230 μg/L). These findings indicated hypophosphatemia and hyperphosphaturia (increased levels of ALP). However, because the patient had normal levels of 1,25-dihydroxyvitamin D3, we considered that the impaired phosphate reabsorption could have been caused by dysfunction of the proximal renal tubule dysfunction and not by deficiency of vitamin D. Urinalysis and examination of urine samples collected over 24 h showed increased levels of *N*-acetylglucosaminidase and β2-microglobulin as well as phosphate wasting, which also indicated that these symptoms were caused by dysfunction of the proximal renal tubule.

On the basis of these findings, we made a diagnosis of osteomalacia and pathologic fractures due to Fanconi's syndrome secondary to adefovir therapy (10 mg/day). We conducted preoperative examinations to perform total hip arthroplasty. Prolonged bleeding time was observed by platelet aggregation failure and coagulation factor deficiency (Table 1). The coagulation disorder was suggested to have been caused by chronic hepatitis. The bleeding time was normalized by platelet transfusion. or double-labeling analysis, 1000 mg of tetracycline was orally

Table 1 Title: coagulation factors

	Activity	Normal range
Coagulation factor II	46.6%	(66.0–118.0)
Coagulation factor III	65.1%	(73.0–122.0)
Coagulation factor VII	65.6%	(54.0–162.0)
Coagulation factor VIII	89.8%	(78.0–165.0)
Coagulation factor IX	43.5%	(67.0–152.0)
Coagulation factor X	54.3%	(58.0–200.0)
Coagulation factor XI	43.5%	(75.0–137.0)
Von Willebrand factor	200%	(50.0–150.0)

administered at 10-day intervals. A 2-step procedure was performed under the same general anesthetic. During the first part of the procedure, biopsy of the iliac bone was performed, and during the second stage of the procedure, total hip arthroplasty was performed using a Zimmer implant (cemented collarless polished taper. stem, cementless trabecular metal modular acetabular cup, 36-mm head; Figure 1d). Because the acetabular roof bone was too fragile to support the acetabular components, bone fragment autografts prepared from the left femoral head were transplanted at the acetabular roof. The patient received intravenous antibiotics for 3 days. On the first postoperative day, the patient began rehabilitation under the supervision of a physiotherapist. He began using crutches for ambulation on postoperative day 7, with progressive weight-bearing as tolerated. The time to full weight-bearing was 3 weeks after the operation. The iliac bone and femoral head samples were fixed and stained using Villanueva bone stain and Villanueva–Goldner counterstain. The osteoid volume/mineralized bone volume ratio was 20.7% (average, <10%) and osteoid thickness was 25.1 μm (average, <12.5 μm; Figure 2a). Examination using tetracycline labeling showed no double-labeling pattern (Figure 2b) [8]. These findings confirmed that the pathological fractures were caused by osteomalacia (reviewed in [8]). After surgery, adefovir dipivoxil was switched with entecavir hydrate, and eldecalcitol and alendronate sodium hydrate were administered. These treatments normalized the blood phosphate level. The Japanese Orthopaedic Association Hip Score for the hip joints was 73 points at 2 months after surgery. He did not show any new pathological fractures.

Discussion

Adefovir dipivoxil is a commonly used antiviral agent in the treatment of chronic hepatitis B or HIV infection [9]. Fanconi's syndrome has been recognized as a

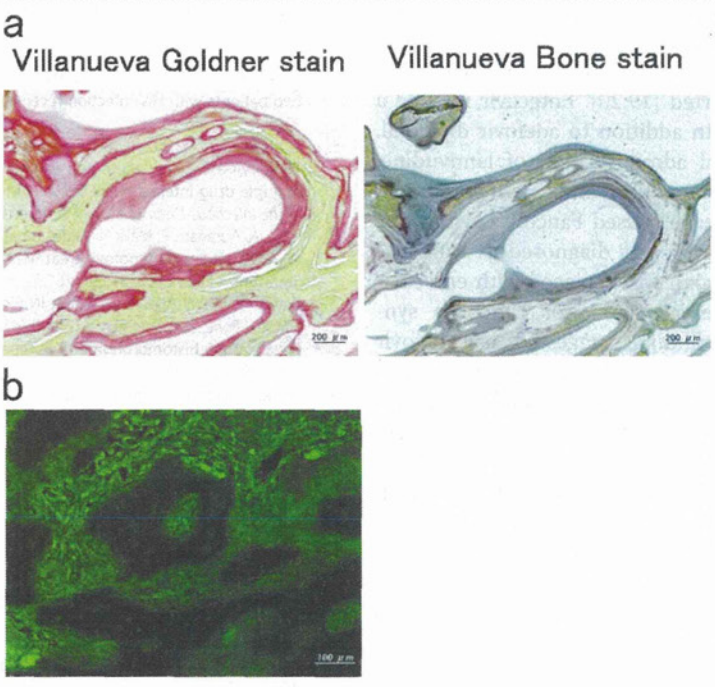

Figure 2 Pathological examinations. a: Mineralized bone tissues are colored in green and nonmineralized osteoid tissues are shown in orange by Villanueva-Goldner stain. Mineralized bone tissues are colored in purple and nonmineralized osteoid tissues are shown in the clear zone by Villanueva bone stain. The osteoids volume/mineralized bone volume ratio was 20.7% (normal range, less than 10%). Osteoid thickness was 25.1 μm (average, less than 12.5 μm). **b**: Tetracycline labeling examination showed no double-labeling pattern. These findings indicate mineralization deficiency and osteomalacia.

complication of high-dose adefovir dipivoxil therapy (dose, 60–120 mg/day) in the treatment of HIV infection [10]. Few studies have reported severe hypophosphatemia with 10 mg/day adefovir dipivoxil therapy [11-14]. In addition, to our knowledge, this is the first report of pathological femoral neck fracture associated with adefovir dipivoxil-induced osteomalacia treated by total hip arthroplasty. When orthopaedic surgeons encounter adefovir dipivoxil–treated chronic hepatitis B patients with pathological hip fractures, the patients' renal function and levels of electrolytes, including calcium and phosphorus, should be carefully monitored.

Fanconi's syndrome results from dysfunction of the proximal renal tubule, causing impaired reabsorption of amino acids, urate, bicarbonate, and phosphate and increased excretion of these solutes into the urine. The pathophysiology of proximal renal tubule dysfunction is thought to be an increase in the adefovir dipivoxil concentration in the mitochondria mediated by inhibition of several ATP-dependent transporters [15,16]. Patients with Fanconi's syndrome show low phosphate levels (because of renal phosphate loss) and normal levels of calcium, 25-hydroxyvitamin D, 1,25-dihydroxyvitamin D, and PTH and increased ALP levels. Radiography and bone scan showed multiple patterns of osteomalacia. Our findings were consistent with those in previous reports [17].

Entecavir is more effective than adefovir dipivoxil, with a favorable safety profile and low incidence of resistance [18]. We switched adefovir dipivoxil with entecavir hydrate as previously reported [19,20]. Entecavir may be a good treatment choice. In addition to adefovir dipivoxil, the patient received oral administration of lamivudine, rebamipide, rabeprazole sodium, and methylprednisolone. These drugs may have caused Fanconi's syndrome. After the patient's condition was diagnosed as Fanconi's syndrome, adefovir dipivoxil was replaced with entecavir hydrate. Thereafter, the symptoms of Fanconi's syndrome improved. These findings suggested that adefovir dipivoxil caused Fanconi's syndrome and osteomalacia.

In conclusion, orthopaedic surgeons should be aware of osteomalacia and pathologic fractures caused by adefovir dipivoxil administered as anti-hepatitis B virus therapy. In addition to the above-mentioned antiviral agent, ifosfamide, valproic acid, aminoglycosides, methyl-3-chromone, paraquat, L-lysine, calcineurin-inhibitor, or tetracycline may cause hypophosphatemic osteomalacia; therefore, serum ALP and phosphorus levels of patients receiving these drugs should be monitored [21-28].

Consent

Written informed consent was obtained from the patient and his family for publication of this case report. A copy of the written consent is available for review by the Editor-in-Chief of the journal.

Abbreviations

HIV: Human immunodeficiency virus; MRI: Magnetic resonance imaging; HMDP: ^{99m}Tc-hydroxymethylene diphosphonate; ALP: Alkaline phosphatase; BUN: Blood urea nitrogen; PTH: Parathyroid hormone.

Competing interests

The authors declare that they have no competing interests.

Authors' contributions

MT, YA, and SN were responsible for data collection. TS, YI, and SK, were responsible for literature search and manuscript preparation. MH, YS, and HK performed microscopic examinations, and JK performed surgery. All authors have read and approved the final manuscript.

Author details

[1]Department of Orthopaedic Surgery, Graduate School of Medical and Dental Sciences, Kagoshima University, Kagoshima, Japan. [2]The Near-Future Locomotor Organ Medicine Creation Course (Kusunoki Kai), Graduate School of Medical and Dental Sciences, Kagoshima University, 8-35-1 Sakuragaoka, Kagoshima 890-8520, Japan. [3]Department of Medical Joint Materials, Graduate School of Medical and Dental Sciences, Kagoshima University, Kagoshima, Japan.

Received: 30 May 2012 Accepted: 28 June 2012
Published: 20 August 2012

References

1. Clarke BL, Wynne AG, Wilson DM, Fitzpatrick LA: **Osteomalacia associated with adult Fanconi's syndrome: clinical and diagnostic features.** *Clin Endocrinol* 1995, **43**:479–490.
2. Verhelst D, Monge M, Meynard JL, Fouqueray B, Mougenot B, Girard PM, Ronco P, Rossert J: **Fanconi syndrome and renal failure induced by tenofovir: a first case report.** *Am J Kidney Dis* 2002, **40**:1331–1333.
3. Earle KE, Seneviratne T, Shaker J, Shoback D: **Fanconi's syndrome in HIV + adults: report of three cases and literature review.** *J Bone Miner Res* 2004, **19**:714–721.
4. Parsonage MJ, Wilkins EG, Snowden N, Issa BG, Savage MW: **The development of hypophosphataemic osteomalacia with myopathy in two patients with HIV infection receiving tenofovir therapy.** *HIV Med* 2005, **6**:341–346.
5. Zimmermann AE, Pizzoferrato T, Bedford J, Morris A, Hoffman R, Braden G: **Tenofovir-associated acute and chronic kidney disease: a case of multiple drug interactions.** *Clinical infectious diseases: an official publication of the Infectious Diseases Society of America* 2006, **42**:283–290.
6. Malik A, Abraham P, Malik N: **Acute renal failure and Fanconi syndrome in an AIDS patient on tenofovir treatment–case report and review of literature.** *J Infect* 2005, **51**:E61–E65.
7. Garden RS: **LOW-ANGLE FIXATION IN FRACTURES OF THE FEMORAL NECK.** *J Bone Joint Surg Br* 1961, **43-B**:647–663.
8. Ott SM: **Bone histomorphometry in renal osteodystrophy.** *Semin Nephrol* 2009, **29**:122–132.
9. Wong T, Girgis CM, Ngu MC, Chen RC, Emmett L, Archer KA, Seibel MJ: **Hypophosphatemic osteomalacia after low-dose adefovir dipivoxil therapy for hepatitis B.** *J Clin Endocrinol Metab* 2010, **95**:479–480.
10. Kahn J, Lagakos S, Wulfsohn M, Cherng D, Miller M, Cherrington J, Hardy D, Beall G, Cooper R, Murphy R, *et al*: **Efficacy and safety of adefovir dipivoxil with antiretroviral therapy: a randomized controlled trial.** *Jama* 1999, **282**:2305–2312.
11. Izzedine H, Kheder-Elfekih R, Housset P, Sarkozy C, Brocheriou I, Deray G: **Adefovir dipivoxil-induced acute tubular necrosis and Fanconi syndrome in a renal transplant patient.** *AIDS (London, England)* 2009, **23**:544–545.
12. Jung YK, Yeon JE, Choi JH, Kim CH, Jung ES, Kim JH, Park JJ, Kim JS, Bak YT, Byun KS: **Fanconi's syndrome associated with prolonged adefovir dipivoxil therapy in a hepatitis B virus patient.** *Gut and Liver* 2010, **4**:389–393.
13. Minemura M, Tokimitsu Y, Tajiri K, Nakayama Y, Kawai K, Kudo H, Hirano K, Atarashi Y, Yata Y, Yasumura S, *et al*: **Development of osteomalacia in a post-liver transplant patient receiving adefovir dipivoxil.** *World J Hepatol* 2010, **2**:442–446.
14. Lee HJ, Choi JW, Kim TN, Eun JR: **A case of severe hypophosphatemia related to adefovir dipivoxil treatment in a patient with liver cirrhosis**

related to hepatitis B virus. *The Korean Journal of Hepatology* 2008, **14**:381–386.
15. Tanji N, Tanji K, Kambham N, Markowitz GS, Bell A, D'Agati VD: **Adefovir nephrotoxicity: possible role of mitochondrial DNA depletion.** *Hum Pathol* 2001, **32**:734–740.
16. Cihlar T, Lin DC, Pritchard JB, Fuller MD, Mendel DB, Sweet DH: **The antiviral nucleotide analogs cidofovir and adefovir are novel substrates for human and rat renal organic anion transporter 1.** *Mol Pharmacol* 1999, **56**:570–580.
17. Izzedine H, Launay-Vacher V, Isnard-Bagnis C, Deray G: **Drug-induced Fanconi's syndrome.** *Am J Kidney Dis* 2003, **41**:292–309.
18. Asselah T, Lada O, Boyer N, Martinot M, Marcellin P: **Treatment of chronic hepatitis B.** *Gastroenterol Clin Biol* 2008, **32**:749–768.
19. Lai CL, Rosmawati M, Lao J, Van Vlierberghe H, Anderson FH, Thomas N, Dehertogh D: **Entecavir is superior to lamivudine in reducing hepatitis B virus DNA in patients with chronic hepatitis B infection.** *Gastroenterology* 2002, **123**:1831–1838.
20. Chang TT, Gish RG, Hadziyannis SJ, Cianciara J, Rizzetto M, Schiff ER, Pastore G, Bacon BR, Poynard T, Joshi S, *et al*: **A dose-ranging study of the efficacy and tolerability of entecavir in Lamivudine-refractory chronic hepatitis B patients.** *Gastroenterology* 2005, **129**:1198–1209.
21. Melnick JZ, Baum M, Thompson JR: **Aminoglycoside-induced Fanconi's syndrome.** *Am J Kidney Dis* 1994, **23**:118–122.
22. Yoshikawa H, Watanabe T, Abe T: **Fanconi syndrome caused by sodium valproate: report of three severely disabled children.** *Eur J Paediatr Neurol* 2002, **6**:165–167.
23. Otten J, Vis HL: **Acute reversible renal tubular dysfunction following intoxication with methyl-3-chromone.** *J Pediatr* 1968, **73**:422–425.
24. Vaziri ND, Ness RL, Fairshter RD, Smith WR, Rosen SM: **Nephrotoxicity of paraquat in man.** *Arch Intern Med* 1979, **139**:172–174.
25. Lo JC, Chertow GM, Rennke H, Seifter JL: **Fanconi's syndrome and tubulointerstitial nephritis in association with L-lysine ingestion.** *Am J Kidney Dis* 1996, **28**:614–617.
26. Varavithya W, Chulajata R, Ayudthya PS, Preeyasombat C: **Fanconi syndrome caused by degraded tetracycline.** *J Med Assoc Thail= Chotmaihet thangphaet* 1971, **54**:62–67.
27. Negro A, Regolisti G, Perazzoli F, Davoli S, Sani C, Rossi E: **Ifosfamide-induced renal Fanconi syndrome with associated nephrogenic diabetes insipidus in an adult patient.** *Nephrol Dial Transplant* 1998, **13**:1547–1549.
28. Morard I, Mentha G, Spahr L, Majno P, Hadengue A, Huber O, Morel P, Giostra E: **Long-term renal function after liver transplantation is related to calcineurin inhibitors blood levels.** *Clin Transplant* 2006, **20**:96–101.

doi:10.1186/1746-1596-7-108
Cite this article as: Tanaka *et al.*: Pathological femoral fractures due to osteomalacia associated with adefovir dipivoxil treatment for hepatitis B: a case report. *Diagnostic Pathology* 2012 **7**:108.

Submit your next manuscript to BioMed Central and take full advantage of:

- Convenient online submission
- Thorough peer review
- No space constraints or color figure charges
- Immediate publication on acceptance
- Inclusion in PubMed, CAS, Scopus and Google Scholar
- Research which is freely available for redistribution

Submit your manuscript at
www.biomedcentral.com/submit

BioMed Central

THE JOURNAL OF BIOLOGICAL CHEMISTRY VOL. 287, NO. 34, pp. 29101–29113, August 17, 2012
© 2012 by The American Society for Biochemistry and Molecular Biology, Inc. Published in the U.S.A.

SnoN Suppresses Maturation of Chondrocytes by Mediating Signal Cross-talk between Transforming Growth Factor-β and Bone Morphogenetic Protein Pathways*[S]

Received for publication, February 2, 2012, and in revised form, June 21, 2012 Published, JBC Papers in Press, July 5, 2012, DOI 10.1074/jbc.M112.349415

Ichiro Kawamura[‡§], Shingo Maeda[‡1], Katsuyuki Imamura[‡§], Takao Setoguchi[¶], Masahiro Yokouchi[§], Yasuhiro Ishidou[‡], and Setsuro Komiya[‡§]

From the [‡]Department of Medical Joint Materials, [§]Department of Orthopedic Surgery, and the [¶]Near-Future Locomotor Organ Medicine Creation Course, Graduate School of Medical and Dental Sciences, 8-35-1 Sakuragaoka, Kagoshima University, Kagoshima 890-8544, Japan

Background: BMP signaling promotes chondrocyte maturation and, subsequently, endochondral ossification, whereas TGF-β signaling is inhibitory.
Results: TGF-β induced SnoN to suppress BMP signaling and chondrocyte hypertrophy.
Conclusion: SnoN mediates a signal cross-talk between TGF-β and BMP to regulate chondrocyte maturation.
Significance: Our data revealed an effector of TGF-β signaling as a putative therapeutic molecular target for cartilage/bone regeneration or osteoarthritis.

Hypertrophic maturation of chondrocytes is a crucial step in endochondral ossification, whereas abnormally accelerated differentiation of hypertrophic chondrocytes in articular cartilage is linked to pathogenesis of osteoarthritis. This cellular process is promoted or inhibited by bone morphogenetic protein (BMP) or transforming growth factor-β (TGF-β) signaling, respectively, suggesting that these signaling pathways cross-talk during chondrocyte maturation. Here, we demonstrated that expression of *Tgfb1* was increased, followed by phosphorylation of Smad2, during BMP-2-induced hypertrophic maturation of ATDC5 chondrocytes. Application of a TGF-β type I receptor inhibitor compound, SB431542, increased the expression of *Id1*, without affecting the phosphorylation status of Smad1/5/8, indicating that the activated endogenous TGF-β pathway inhibited BMP signaling downstream of the Smad activation step. We searched for TGF-β-inducible effectors that are able to inhibit BMP signaling in ATDC5 cells and identified SnoN. Overexpression of SnoN suppressed the activity of a BMP-responsive luciferase reporter in COS-7 cells as well as expression of *Id1* in ATDC5 cells and, subsequently, the expression of *Col10a1*, a hallmark of hypertrophic chondrocyte maturation. siRNA-mediated loss of SnoN showed opposite effects in BMP-treated ATDC5 cells. In adult mice, we found the highest level of *SnoN* expression in articular cartilage. Importantly, SnoN was expressed, in combination with phosphorylated Smad2/3, in prehypertrophic chondrocytes in the growth plate of mouse embryo bones and in chondrocytes around the ectopically existing hypertrophic chondrocytes of human osteoarthritis cartilage. Our results indicate that SnoN mediates a negative feedback mechanism evoked by TGF-β to inhibit BMP signaling and, subsequently, hypertrophic maturation of chondrocytes.

Bone formation is achieved by either intramembranous or endochondral ossification. The former process is characterized by differentiation of mesenchymal cells directly into bone-forming osteoblasts. Endochondral ossification is initiated by condensation of mesenchymal cells expressing a chondrogenic master regulator, *Sox9*, after which cells further differentiate into chondrocytes that are able to express a specific marker *Col2a1*, encoding type II collagen (1). Then the committed chondrocytes proliferate and convert into hypertrophic chondrocytes to eventually mineralize the surrounding cartilage matrix to be replaced by bone (2). Hypertrophic chondrocytes are characterized by a round large cell body and the ability to express *Col10a1*, encoding type X collagen. This hypertrophic conversion process is, at least in part, governed by Runx2 protein (*i.e.* Runx2 directly activates the promoter of *Col10a1* to promote chondrocyte hypertrophy) (3, 4). Mouse models in which dominant-negative Runx2 was overexpressed in chondrocytes showed suppressed chondrocyte hypertrophy, combined with complete loss of endochondral ossification (5). Conversely, forced expression of wild-type Runx2 in mouse chondrocytes resulted in accelerated differentiation of hypertrophic chondrocytes and bone formation (5, 6). Given that in permanent cartilage (*e.g.* normal articular cartilage on the joint space), chondrocytes do not undergo the late phase hypertrophic maturation, hypertrophic conversion of chondrocytes must be restricted to maintain a normal cartilage phenotype.

In addition to its indispensable role in physiological bone formation, the endochondral ossification process is a promising cellular event in the application of bone/cartilage regenerative medicine, which can be artificially engineered from human mesenchymal stem/stroma cells (7). Interestingly, these mesenchymal stem/stroma cells form bone trabeculae *in vivo* only

* This work was supported by Grants-in-Aid for Scientific Research (Scientific Research (C) (General)) 23592221 (to S. M.) and 23592222 (to Y. I.) and Japan Orthopedics and Traumatology Foundation, Inc., Grant 254.
[S] This article contains supplemental Table 1 and Fig. 1.
[1] To whom correspondence should be addressed. Tel.: 81-99-275-5381; Fax: 81-99-265-4699; E-mail: s-maeda@m3.kufm.kagoshima-u.ac.jp.

when they have developed hypertrophic structures *in vitro* before implantation (7), indicating that the efficiency of bone regeneration could be improved by promoting hypertrophic maturation of chondrocytes *in vitro*. In the case of cartilage regenerative medicine for treatment of cartilage defects, the maturation processes in engineered chondrocytes must be arrested because abnormally matured hypertrophic chondrocytes, expressing type X collagen, cause pathological conditions (*e.g.* osteoarthritis (OA)[2]) (8–10). *In vitro*, mesenchymal stem/stroma cells rapidly express *COL10A1* in monolayer or pellet culture before the cells demonstrate morphology of hypertrophic chondrocytes, a phenomenon that is a major problem of cartilage tissue engineering (11, 12), suggesting that the mechanism by which mesenchymal stem/stroma cells induce type X collagen is different from that in growth plate chondrocytes. Importantly, it is largely unknown how the expression of type X collagen is induced in degenerating articular chondrocytes.

Both BMP and TGF-β signaling promote early chondrogenesis. Members of the TGF-β family, including BMPs, transduce signals through type II and type I receptors to activate receptor-regulated Smads (R-Smads). Upon ligand binding, TGF-β type I receptors activate Smad2/3, whereas BMP type I receptors phosphorylate Smad1/5/8 in the cytoplasm. After forming a trimeric complex with Smad4 (co-Smad), R-Smads translocate into the nucleus to directly or indirectly regulate the transcription of target genes (13). Forced expression of an extracellular BMP-antagonist, Noggin (*Nog*), in chondrocytes *in vivo* showed no cartilage formation in transgenic mice (14). Similarly, cartilage-specific combined loss of BMP type I receptors (*Bmpr1a* and *Bmpr1b*) or double deletions of BMP-type R-Smads (*Smad1* and *Smad5*) showed severely impaired chondrogenesis in mice (15, 16). These mouse models clearly demonstrated the critical roles of the BMP-Smad pathway in early chondrogenesis. TGF-β signaling promotes the early stage of chondrogenesis by enabling Smad3 to form an active transcriptional complex with CEBP/p300 and Sox9 (17). However, at the late maturation stage, BMP and TGF-β signaling show mutually opposite roles in chondrocyte hypertrophy. BMP signaling directly accelerates the expression of *Col10a1* in concert with Runx2 (18–20), whereas the chondrocyte-specific expression of constitutively active *Bmpr1a* promoted the maturation and hypertrophy of chondrocytes in transgenic mice (21). An intra-articular injection of BMP-2 in mice accelerated cartilage chondrocyte hypertrophy and endochondral ossification to form osteophytes, a phenotype of OA (22). In contrast, loss of TGF-β signaling in the cartilage of mice, achieved by targeted ablation of the *Smad3* gene or forced expression of the dominant negative TGF-β type II receptor, resulted in accelerated differentiation of chondrocytes into hypertrophy coupled with an OA-like destruction of cartilage (23, 24). Similarly, chondrocyte-specific transgenic mice of Smurf2, an E3 ubiquitin ligase of the negative regulator for TGF-β signaling, also showed an OA-like change in articular cartilage with ectopic hypertrophic chondrocytes (25). These mouse models indicated an indispensable role of TGF-β signaling in preventing chondrocyte hypertrophy in articular cartilage, although the underlying molecular mechanisms are unclear. Interestingly, Smad3-deficient chondrocytes showed enhanced BMP signaling and accelerated hypertrophic differentiation *in vitro*, suggesting a role of endogenous TGF-β signaling in suppressing BMP signaling during chondrocyte maturation (26). Taken together, promoting TGF-β signaling in maturing chondrocytes is a promising candidate approach to manipulate the differentiation to fine tune chondrocyte hypertrophy. However, because TGF-β signaling regulates a wide range of pivotal biological functions (*e.g.* cell growth, differentiation, motility, extracellular matrix production, and apoptosis) in various target cells, blocking of the entire TGF-β signaling pathway might result in undesirable side effects. Therefore, to eliminate these problems, the direct mediator(s) induced by TGF-β signaling to inhibit BMP signaling in maturing chondrocytes should be an appropriate molecular target. Here, we show that SnoN is as a spatial and temporal effector of TGF-β signaling to inhibit the BMP-Smad pathway and, subsequently, chondrocyte hypertrophy.

EXPERIMENTAL PROCEDURES

Cell Culture—The chondrogenic cell line ATDC5 was obtained from RIKEN BioResource Center. The cells were maintained in Dulbecco's modified Eagle's medium (DMEM)/Ham's F-12 (1:1) (Invitrogen) containing 5% fetal bovine serum (FBS) and 100 units/ml penicillin G and 100 μg/ml streptomycin. Differentiation of ATDC5 cells was induced in serum-free medium containing insulin/transferrin/selenium supplement (Sigma) on collagen type I-coated culture plates (Iwaki). For expression analysis of differentiation markers in ATDC5 cells, micromass culture was performed as previously described (27), to accelerate maturation of chondrocyte differentiation. A monolayer culture system was employed for analysis of phosphorylation of Smads by immunoblotting because the cell lysis of micromass culture for cytoplasmic/nuclear protein was less efficient, and in addition, these experiments were not intended to evaluate the chondrogenic differentiation of early time points but rather the intracellular signaling. Monolayer culture was also performed for immunocytochemistry because of the difficulty in identifying individual cells in the micromass culture. Primary chondrocytes were harvested from 4-day-old mice of C57BL/6J background as described (28). Primary chondrocytes were induced to differentiate in a monolayer culture. COS-7 cells were purchased from the RIKEN BioResource Center and maintained in DMEM supplemented with 10% FBS and antibiotics.

Ligands and Inhibitors—BMP-2 (Peprotech) was applied at a concentration of 300 ng/ml, whereas TGF-β1 (Peprotech) was used at 5 ng/ml. The day of the first ligand application was referred to as day 0. SB431542 (Sigma) was applied at 1 μM for 30 min prior to ligand stimulation, and DMSO was used as a mock control. When indicated, cells were treated with a proteasome inhibitor, MG132 (Merck), at 10 μM 12 h prior to cell lysis.

Bone Organ Culture—Metatarsal bone rudiments were harvested from C57BL/6J embryos at 17.5 days postcoitum (E17.5) and cultured in DMEM supplemented with 10% FBS, 100

[2] The abbreviations used are: OA, osteoarthritis; BMP, bone morphogenetic protein; qPCR, quantitative PCR; E17.5, embryonic day 17.5.

units/ml penicillin G, and 100 μg/ml streptomycin, as described (29). Cultured bones were stained with Alcian blue and alizarin red dyes according to a standard protocol for skeletal preparation. Briefly, bones fixed in 96% ethanol were stained with 0.015% Alcian blue 8GX (Sigma) in a mixture solution of 96% ethanol, acetic acid (4:1) for 1 day, followed by a dehydration step in 100% ethanol. Dehydrated bones were immersed briefly in 1% potassium hydroxide (KOH), followed by staining in 0.001% alizarin red S (Sigma) in 1% KOH for 1 day. Images were analyzed using ImageJ software (National Institutes of Health). Animal experiments were approved by the Institutional Animal Care and Use Committee of Kagoshima University (MD11019).

RNA Interference—Dharmacon siRNA ON-TARGETplus SMARTpool, a mixture of four independent siRNAs of mouse SnoN (*Skil*), and the control reagent were purchased from Thermo Scientific. siRNA was transfected into cells using Lipofectamine RNAiMax (Invitrogen). Ligands and SB431542 were added to the culture simultaneously after an overnight transfection of siRNA.

Plasmids—9xCAGA luc, BRE luc, ALK5TD, ALK3QD, and FLAG-tagged human SnoN in pcDEF3 were kind gifts from Dr. Kohei Miyazono (University of Tokyo). pGL4.75hRlucCMV was purchased from Promega. cDNA of mouse SnoN was cloned from ATDC5 by employing a reverse transcription-polymerase chain reaction (RT-PCR)-based technique, subcloned into the entry vector, pENTR, and further transferred into pEF-DEST51 by attL-attR (LR) recombination (Invitrogen).

Lentivirus—pENTR-SnoN and pENTR-5′EF1αP were subjected to LR recombination with pLenti6.4/R4R2/V5-DEST (Invitrogen) to generate a lentiviral vector, which expresses C-terminal V5-tagged *SnoN* from the EF1α promoter. The lentiviral expression vector or pLenti6/V5/GW-lacZ control vector was transfected into 293FT cells to generate lentivirus. The conditioned medium containing lentivirus was incubated with mouse metatarsal bones for 16 h for infection. The infection efficiency was monitored by immunohistochemistry on the coronal section of infected bones using anti-V5-FITC antibody.

Immunoblotting—Cells were lysed in either M-PER lysis buffer (Thermo Scientific) supplemented with aprotinin, sodium orthovanadate, and phenylmethylsulfonyl fluoride (PMSF) or directly with 1× SDS sample buffer. SDS-PAGE, membrane transfer, and chemiluminescence were performed by using a standard protocol. Blots were incubated with anti-SnoN (1:200, H-317, sc-9142, Santa Cruz Biotechnology, Inc. (Santa Cruz, CA)), anti-phospho-Smad1/5/8 (1:1000, catalog no. 9511), anti-phospho-Smad2 (1:1000, catalog no. 3108), anti-Smad1 (1:1000, catalog no. 9743), horseradish peroxidase (HRP)-conjugated anti-rabbit secondary antibody and anti-mouse secondary antibody (1:10,000) (Cell Signaling), anti-Smad2/3 (1:1000, catalog no. 610842, BD Biosciences), anti-tubulin (1:1000, DM1A, T9026, Sigma), and anti-Mmp13 (1:1000, ab58836, Abcam). Signals were detected using the LAS 4000 mini image analyzer (Fujifilm).

Immunocytochemistry and Immunohistochemistry—For immunocytochemistry, cells were fixed with 4% paraformaldehyde in PBS for 30 min and treated with 0.2% Triton X-100. For antigen retrieval of type X collagen, cells were digested with 5 units/ml hyaluronidase (Calbiochem) for 30 min at 37 °C, followed by pepsin (Quartett) digestion for 15 min at 37 °C. CAS block (Zymed Laboratories Inc.) was used for blocking. Cells were incubated with anti-type X collagen (1:50, LB-0092, LSL), anti-SnoN (1:50, H-317, sc-9142, Santa Cruz Biotechnology, Inc.), anti-phospho-Smad2 (1:100, catalog no. 3108, Cell Signaling), and anti-Smad2/3 (1:100, catalog no. 610842, BD Biosciences). Anti-rabbit Alexa Fluor 488 (1:200, A11008), or anti-mouse Alexa Fluor 546 (1:200, A11060) (Invitrogen) was used to detect signals. Normal rabbit or mouse serum was used as negative control. For immunohistochemistry, we obtained human samples from individuals undergoing total hip arthroplasty after obtaining written informed consent as approved by the Ethics Committee of Kagoshima University (number 22-85). Formalin-fixed human femoral heads, mouse E17.5 embryo humeri, or bone organ culture were embedded in paraffin blocks, which were sliced at 4-μm thickness. The antigen was retrieved by using L.A.B. (Liberate Antibody Binding) solution (Polysciences), except in the case of type X collagen antigen retrieval with hyaluronidase digestion. CAS block was used for blocking except for the cultured bones, which were blocked by using 5% bovine serum albumin in PBS. Blocked sections were incubated with anti-type X collagen (1:50, LB-0092, LSL), anti-TGF-β1 (1:50, sc146, Santa Cruz Biotechnology, Inc.), anti-phospho-Smad2 (1:100, catalog no. 3103, Cell Signaling), anti-phospho-Smad3 (1:500, catalog no. 600-401-919, Rockland), anti-Smad2/3 (1:100, catalog no. 610842, BD Biosciences), anti-SnoN (1:50, H-317, sc-9142, Santa Cruz Biotechnology, Inc.), and anti-V5-FITC (1:50, R963-25, Invitrogen). Signals were detected using the REAL EnVision detecting system with DAB chromogen (Dako), anti-rabbit Alexa Fluor 488 (1:200, A11008), or anti-mouse Alexa Fluor 546 (1:200, A11060) (Invitrogen).

Real-time Quantitative PCR Assay—Cells were lysed with the TRIzol reagent (Invitrogen) to purify RNA, and 1 μg of RNA was reverse transcribed into cDNA by using the Verso cDNA Kit (Thermo Scientific). The relative amount of gene transcripts was determined by real-time PCR using the THUNDERBIRD quantitative PCR (qPCR) mix (Toyobo) on the Thermal Cycler Dice TP850 (Takara). PCRs were performed in duplicate, and the measured expression level of each gene was normalized to that of *Hprt1*. Sequence information of primers used is listed in supplemental Table 1.

Luciferase Assay—COS-7 cells were seeded in triplicate in 24-well plates and transiently transfected with firefly reporter constructs, pGL4.75hRlucCMV *Renilla* vector, constitutively active type I receptor constructs, and the SnoN vector. Dual luciferase assays were performed as described (30) using the GloMax 96 microplate luminometer (Promega).

Statistical Analysis—Data in this study are expressed as the mean ± S.D. of at least three independent experiments. A p value of <0.05, which was determined by Student's t test, was accepted as statistically significant.

RESULTS

Endogenous TGF-β Signaling Suppresses Terminal Chondrocyte Maturation in Bone—To identify physiologically active target genes of TGF-β signaling in chondrocytes, we employed

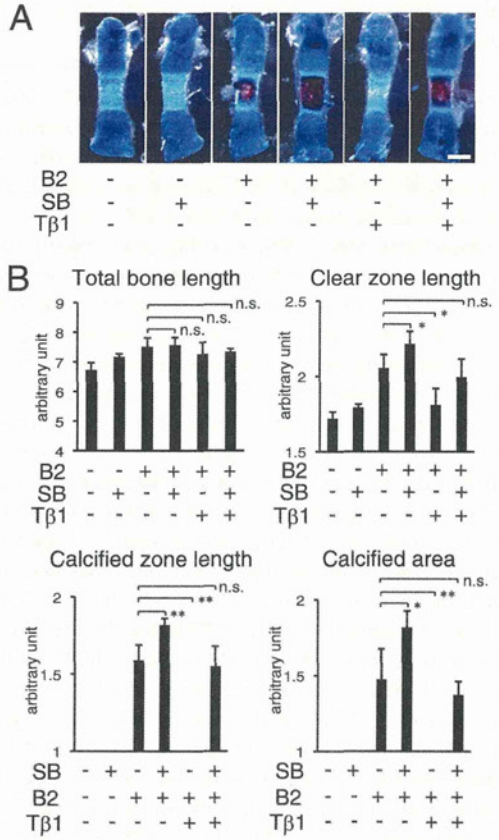

FIGURE 1. **Endogenous TGF-β signaling prevents maturation of chondrocytes in bone organ culture.** Metatarsal bones from E17.5 mouse embryo were cultured with BMP-2 (*B2*; 300 ng/ml) or TGF-β1 (*Tβ1*; 5 ng/ml) in combination with SB431542 (*SB*; 1 μM) for 4 days. *A*, cartilage matrix was stained with Alcian blue, whereas chondrocyte matrix calcified by mature hypertrophic chondrocytes was stained by alizarin red. The clear zone represented hypertrophic chondrocytes. *B*, total bone length, clear zone length, calcified zone length, and calcified area, were analyzed on images using ImageJ software ($n = 4$). *, $p < 0.05$; **, $p < 0.01$; *n.s.*, not significant. *Error bars*, S.D.

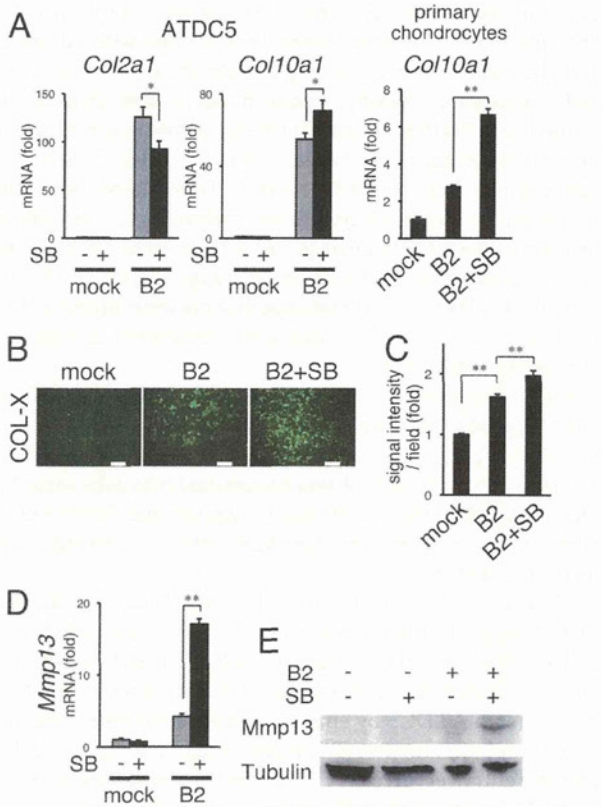

FIGURE 2. **Loss of TGF-β signaling promotes hypertrophic conversion of chondrocytes.** *A*, expression of *Col2a1* and *Col10a1* in ATDC5 chondrocytes and mouse primary chondrocytes was analyzed by qPCR. Cells were treated with or without BMP-2 (*B2*; 300 ng/ml) in combination with SB431542 (*SB*; 1 μM). ATDC5 cells were harvested at day 5, whereas primary chondrocytes were harvested at day 14. *B* and *C*, immunocytochemistry for type X collagen (*COL-X*) was performed on micromass cultures of ATDC5 cells at day 10. *Scale bars*, 200 μm. The fluorescent signal of immunocytochemistry was quantified by ImageJ software for four independent fields per group (*C*). *D*, expression of *Mmp13* mRNA was evaluated by qPCR. *E*, expression of Mmp13 protein in ATDC5 cells at day 18 was assessed by immunoblotting. Tubulin served as a loading control. *, $p < 0.05$; **, $p < 0.01$. *Error bars*, S.D.

a TGF-β type I receptor kinase inhibitor, SB431542, to block endogenous TGF-β signaling. First, we evaluated if SB431542 could accelerate chondrocyte hypertrophy and, subsequently, matrix calcification in mouse embryonic metatarsal bone organ cultures, which is a system that allows for the study of complex chondrogenic processes in a three-dimensional structure in the context of native cell-cell and cell-extracellular matrix interactions and cellular signaling (29). The cartilage matrix was stained by Alcian blue, whereas the matrix calcified by mature hypertrophic chondrocytes was stained by alizarin red; the clear zone represented uncalcified hypertrophic chondrocytes (Fig. 1*A*). Upon treatment with BMP-2, matrix calcification was induced, whereas coapplication of TGF-β1 prevented the chondrocyte maturation. Blocking of endogenous TGF-β signaling by SB431542 in BMP-treated bone significantly enhanced the length of the clear zone as well as both length and area of the calcified matrix of cartilage; this effect was diminished by exogenous TGF-β1 application (Fig. 1, *A* and *B*). The longitudinal bone growth was slightly promoted by BMP-2, whereas SB431542 or TGF-β1 showed no effect. These results confirmed the inhibitory action of endogenous TGF-β signaling in chondrocyte hypertrophy and maturation in bone rudiments.

Next, to investigate cell-autonomous actions of endogenous TGF-β signaling in BMP-induced maturation of chondrocytes, we applied SB431542 in a chondrocyte micromass culture, which is a system widely employed to study the multiple steps of cartilage differentiation (31). Upon treatment with BMP-2 in the presence of insulin/transferrin/selenium supplements, expression of *Col2a1* and *Col10a1* was induced in ATDC5 cells, as reported previously (32), whereas combined application of SB431542 mildly suppressed the level of *Col2a1* mRNA, suggesting the promotive role of TGF-β signaling in early chondrogenesis (Fig. 2*A*). In contrast, BMP-induced expression of *Col10a1* was further enhanced by SB431542 in ATDC5 cells as well as dramatically enhanced in mouse primary chondrocytes (Fig. 2*A*). Whereas treatment with BMP-2 accelerated the production of the type X collagen protein (encoded by *Col10a1*) in ATDC5 cells, SB431542 further strengthened the signal (Fig. 2*B*). The fluorescent signal of immunocytochemistry against type X collagen was significantly increased by SB431542 treat-

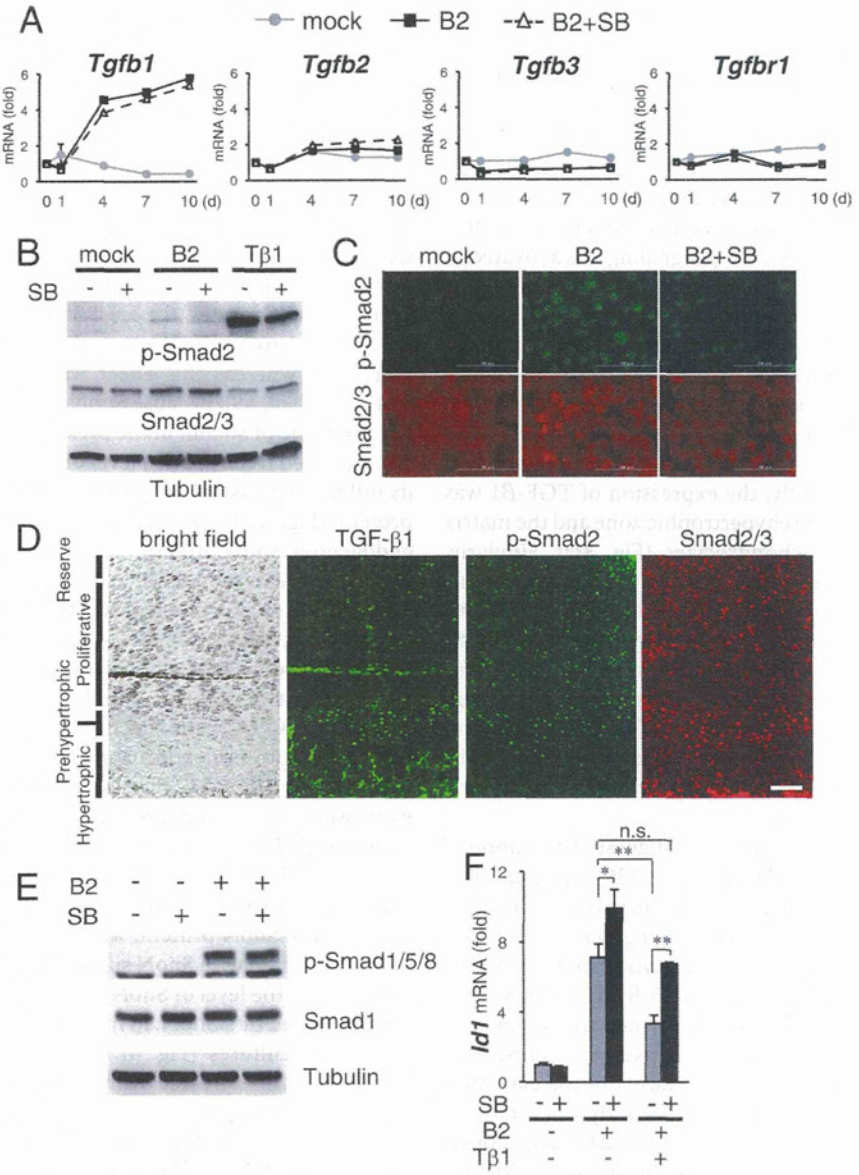

FIGURE 3. **Endogenous TGF-β signaling is activated in maturing chondrocytes to suppress the expression of *Id1*, a direct target gene of BMP-Smad pathway.** *A*, ATDC5 chondrocytes were cultured with BMP-2 (*B2*; 300 ng/ml) in combination with SB431542 (*SB*; 1 μM) for the indicated times. Expression of *Tgfb1*, *Tgfb2*, *Tgfb3*, and *Tgfbr1* were examined by qPCR. *B*, status of TGF-β signaling activity was evaluated by immunoblotting for phosphorylated Smad2 (*p-Smad2*). ATDC5 cells were stimulated with BMP-2 for 7 days or TGF-β1 (*Tβ1*; 5 ng/ml) for 1 h, with or without SB431542. Immunoblot for tubulin served as loading control. *C*, status of TGF-β signaling activity was evaluated by immunocytochemistry for phosphorylated Smad2. ATDC5 cells were stimulated with BMP-2 for 4 days with or without SB431542. *D*, expression of TGF-β1 and status of intracellular TGF-β signaling activity (*p-Smad2*) in mouse E17.5 humerus cartilage were evaluated by immunohistochemistry. *E*, status of BMP signaling activity was evaluated by immunoblotting for phosphorylated Smad1/5/8 (*p-Smad1/5/8*). ATDC5 cells were stimulated with BMP-2 for 4 days, with or without SB431542. Immunoblot for tubulin served as loading control. *F*, expression of *Id1* in ATDC5 cells at day 5 of stimulation was evaluated by qPCR. *Scale bar*, 100 μm. *, $p < 0.05$; **, $p < 0.01$; *n.s.*, not significant. *Error bars*, S.D.

ment (Fig. 2*C*). Moreover, the expression of *Mmp13*, encoding the collagenase matrix metallopeptidase 13 specifically expressed by the terminal hypertrophic chondrocytes, was dramatically up-regulated by blockade of the TGF-β signaling pathway at both mRNA and protein levels (Fig. 2, *D* and *E*). These data demonstrate the cell-autonomous inhibitory action of endogenous TGF-β signaling in the late stage of chondrocyte differentiation.

Endogenous TGF-β Signaling Is Up-regulated during Maturation of Chondrocytes—Because SB431542 affected the late stage of chondrocyte differentiation, we assessed if the expression of any of the three TGF-β ligands was increased during BMP-induced maturation of ATDC5 chondrocytes. Although the mRNA levels of *Tgfb2* and *Tgfb3* were marginally changed by application of BMP-2 or SB431542, *Tgfb1* (encoding TGF-β1) was dramatically increased from day 4 and further remained up-regulated by BMP-2 treatment, whereas it was not affected by SB431542 (Fig. 3*A*). Because TGF-β ligands transduce the signal through TGF-β type I receptor ALK5, encoded by *Tgfbr1*, we asked if expression of *Tgfbr1* was accelerated in maturing ATDC5 cells. However, the expression level of *Tgfbr1* was unchanged by BMP-2 application (Fig. 3*A*). Therefore, we